

GAITGen: Disentangled Motion-Pathology Impaired Gait Generative Model – Bringing Motion Generation to the Clinical Domain

Vida Adeli^{1,2,3}, Soroush Mehraban^{1,2,3}, Majid Mirmehdi⁴, Alan Whone⁴, Benjamin Filtjens^{1,2,3}, Amirhossein Dadashzadeh⁴, Alfonso Fasano^{1,3}, Andrea Iaboni^{1,3}, Babak Taati^{1,2,3}

¹University of Toronto ²Vector Institute for Artificial Intelligence

³University Health Network ⁴University of Bristol

<https://vadeli.github.io/GAITGen/>

Abstract

Gait analysis is crucial for the diagnosis and monitoring of movement disorders like Parkinson’s Disease. While computer vision models have shown potential for objectively evaluating parkinsonian gait, their effectiveness is limited by scarce clinical datasets and challenges in collecting large and well-labelled data, impacting model accuracy and risk of bias. To address these gaps, we propose GAITGen, a novel framework that generates realistic gait sequences conditioned on specified pathology severity levels. GAITGen employs a Conditional Residual Vector Quantized Variational Autoencoder to learn disentangled representations of motion dynamics and pathology-specific factors, coupled with Mask and Residual Transformers for conditioned sequence generation. GAITGen generates realistic, diverse gait sequences across severity levels, enriching datasets and enabling large-scale model training in parkinsonian gait analysis. Experiments on our new PD-GaM (real) dataset demonstrate that GAITGen outperforms adapted state-of-the-art models in both reconstruction fidelity and generation quality, accurately capturing critical pathology-specific gait features. A clinical user study confirms the realism and clinical relevance of our generated sequences. Moreover, incorporating GAITGen-generated data into downstream tasks improves parkinsonian gait severity estimation, highlighting its potential for advancing clinical gait analysis.

1. Introduction

Gait analysis is essential in the assessment of movement disorders such as Parkinson’s Disease (PD). Computer vision models have been developed to objectively evaluate parkinsonian gait using videos of older adults walking, representing significant progress toward more accurate and accessible assessments [15, 33, 41, 42, 60]. Despite these advances, current models face several challenges that limit their effectiveness [2]. Developing robust machine learning models re-

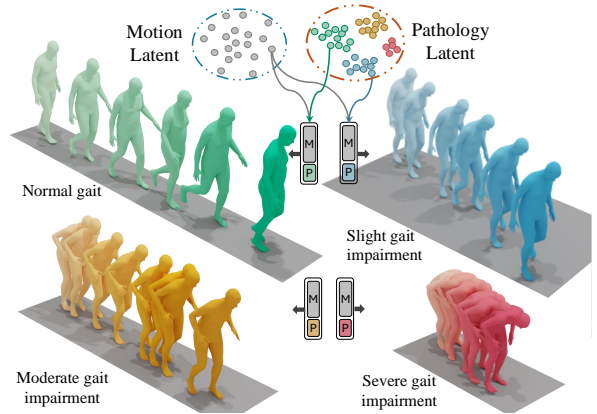


Figure 1. GAITGen disentangles motion and pathology into distinct latents, allowing the same motion dynamics to present differently across pathology latents. This disentanglement enables controlled generation of gait sequences given a pathology level.

quires extensive training data. However, collecting large and diverse gait video datasets is resource-intensive and raises privacy concerns for patients, often resulting in limited and demographically skewed datasets [11, 33, 44, 55]. People with severe parkinsonian gait are particularly underrepresented in these datasets. This scarcity impacts model performance and raises concerns about bias and generalizability across different populations [79]. Moreover, variability in ratings among clinicians introduces inconsistencies in gait severity scoring, affecting the reliability of ground truth labels used for training and evaluation [13, 57]. The severity of gait impairments in PD is commonly assessed using the Unified Parkinson’s Disease Rating Scale (UPDRS) [20]. We focus on the UPDRS Part III gait subscore, hereafter referred to as UPDRS-gait. This scale rates symptoms on a scale from 0 (normal) to 4 (severe impairment). Some of the gait symptoms of PD include small steps and shuffling gait, slow speed, reduced arm swing, stooped posture, and narrow base of support [30, 46].

Generating clinically relevant gait data conditioned on specific pathology severity levels could address existing challenges by augmenting limited real datasets, especially for

underrepresented severe cases. However, this task poses significant difficulties due to the complexity of capturing pathology-specific characteristics and ensuring the generated data is clinically relevant. Existing motion generative models [9, 23, 53] fail to capture nuanced gait deviations associated with movement disorders. Moreover, while large datasets exist for general motion tasks [22, 54], none are suited for generating motions that capture pathology-specific characteristics of impaired gait. Existing gait abnormality datasets are typically small [55] and not formatted for these generative models. Additionally, there is no prior work on generating clinically relevant motions, and standard text-to-motion evaluation metrics previously used [9, 69] are inadequate for this specialized task. To address these gaps, new clinically relevant metrics need to be introduced that assess targeted pathological characteristics, with the flexibility to be adapted for other clinically significant factors. This paper establishes a foundation for assessing generative models in clinical motion analysis.

Our proposed model, GAITGen, is the first to approach the clinically relevant task of generating realistic, pathology-conditioned gait sequences. GAITGen employs a Conditional Residual Vector Quantized Variational Autoencoder (RVQ-VAE) with specific mechanisms to enforce disentanglement, along with a Mask Transformer and a Residual Transformer for conditioned sequence generation. This disentanglement further allows us to leverage motions with mild or moderate impairment and impose severe impairment characteristics, effectively augmenting the dataset with diverse samples across all severity levels (Fig. 1).

Our main contributions are: 1) We propose **GAITGen**, a novel model for generating synthetic, clinically relevant gait sequences conditioned on pathology levels by learning disentangled representation of motion and pathology. This representation also enables Mix and Match augmentation, where pathology characteristics can be superimposed onto different motion profiles. 2) We introduce **PD-GaM**, a public 3D mesh dataset of gait sequences with UPDRS-gait scores along with new evaluation metrics tailored for the pathology-conditioned gait generation task, establishing a foundation for assessing generative models in clinical motion analysis. 3) We validate our model’s clinical relevance and downstream impact through clinician evaluations that confirm the realism and clinical relevance of our synthetic sequences. Using GAITGen-generated data for downstream task improves parkinsonian severity estimation, highlighting its potential utility in clinical applications.

2. Related Works

Human Motion Synthesis. Text-conditioned human motion synthesis has been widely explored in recent work [9, 12, 23, 69, 81, 82]. MDM [69] proposes a conditional diffusion model for motion synthesis. MLD [9] improves MDM’s effi-

ciency using a Variational Autoencoder and compact motion representations. MotionLCM [12] enhances MLD’s runtime with a consistency model and incorporates a motion ControlNet for added control. MoMask [23] proposes a residual VQ-VAE to encode motion into a low-dimensional space and employs a mask modeling transformer for synthesis. OmniControl [78] introduces flexible spatial control across body joints and time steps. While these models generate text-aligned motions effectively, they struggle with clinically specific, unseen patterns like pathological gait. Furthermore, their success depends on exposure to large-scale training data, which limits their applicability to PD datasets where data is inherently scarce.

Human Motion Style Transfer. These methods transfer style from one motion sequence to another while preserving its content [1, 7, 66, 68, 80]. [1] separates motion content and style via dual encoders, using adaptive instance normalization (AdaIN) for style modulation. [7] applies a diffusion model with style control. Style-ERD [68] introduces a real-time online style transfer. MCM-LDM [66] enables arbitrary style transfer by integrating content, style, and trajectory. CycleDance [80] uses a cross-modal transformer for dance style transfer, incorporating music context to enhance realism. Unlike style, pathology in gait is not merely a superficial attribute, but fundamentally affects the underlying motion dynamics and walking biomechanics. Beyond the style of walking, it influences factors such as speed, walking distance, or freezing of gait mid-stride. Modeling pathology as style overlooks these complex interactions, often producing implausible or clinically unrealistic gait sequences.

Disentanglement in Generation. Disentangling two concepts is crucial for precise control over high-quality generation [4, 27, 36, 72–74, 77]. Previous research has shown disentanglement, when used on downstream tasks, enhances performance [38, 39], offers interpretability [25], reduces sample complexity [58, 70], and improves fairness [37]. In generative domain, G³AN [73] disentangles motion and appearance for video generation. DiffSFSR [36] disentangles identity, background, and expression for face generation. DisCo [72] disentangles subject and background in dance synthesis. Though not yet explored in motion generation, we believe disentangling pathology from motion is key for generating clinically accurate motion with limited data.

Synthetic Data as Augmentation. Synthetic data has proven effective in boosting performance with limited real data [29, 50, 62, 62, 74, 75], even when not visually realistic [26, 49]. By disentangling pathology and motion, we produce synthetic gait data that meaningfully improves model accuracy and supports clinical efforts toward earlier PD diagnosis. Prior work [8] used 2D skeletal interpolation to address PD data scarcity, but failed to capture the complexity of parkinsonian gait.

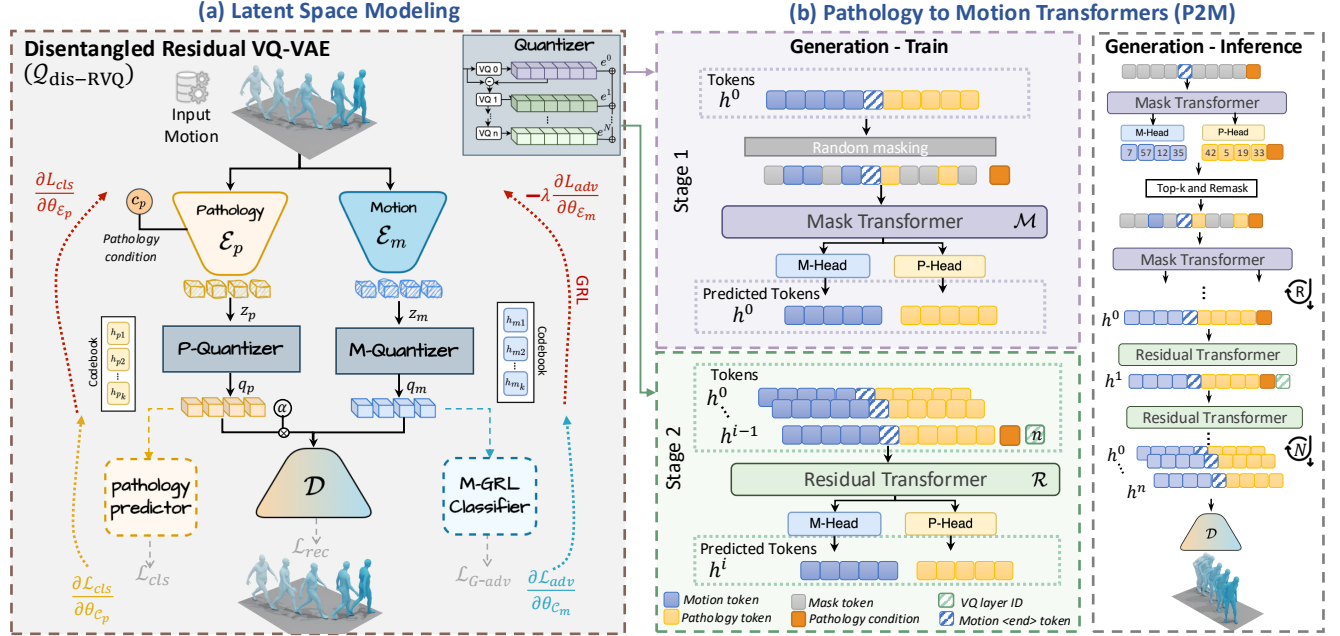


Figure 2. GAITGen architecture. 1) Disentangled Residual VQ-VAE encodes gait sequences into separate motion (\mathcal{E}_m) and pathology (\mathcal{E}_p) latents, enforced by distinct quantizers and classifiers for disentanglement. 2) Generation - Train: In the first stage of training, masked motion and pathology tokens are generated using the Mask Transformer (\mathcal{M}) with separate heads for each latent. In the second stage, the Residual Transformer (\mathcal{R}) predicts residuals with a next layer prediction task. 3) During inference, \mathcal{M} predicts masked tokens iteratively, followed by the \mathcal{R} , which incrementally refines the representations across multiple quantization layers, conditioned on the pathology level.

3. Method

Given a gait sequence $\mathbf{x} \in \mathbb{R}^{T \times D}$ with pathology severity label $c_p \in \{0, \dots, C - 1\}$, where T is the sequence length, D the motion representation dimensionality, and C the number of pathology severity classes (hereafter referred to as “pathology”), our goal is, 1) to learn a disentangled representation that separates motion dynamics from pathology-specific factors while preserving reconstruction fidelity; 2) to build a generative model that synthesizes gait sequences conditioned on pathology levels. To this end, we propose GAITGen, a model that combines a *Conditional* Residual Vector Quantized Variational Autoencoder (RVQ-VAE [35]) with specific mechanisms to enforce disentanglement (Sec. 3.1.1), along with a Mask Transformer (Sec. 3.1.2) and Residual Transformer (Sec. 3.1.3) for conditional gait generation.

3.1. GAITGen Architecture

The overall architecture is shown in Fig. 2. We emphasize why a disentanglement is essential in the first place. Given the limited number of samples in severe pathology classes (often only a few participants), training a generative model to produce diverse motions for these cases is not trivial. By disentangling motion from pathology, we can learn diverse motion patterns from abundant mild cases and impose severe pathology characteristics onto them, enabling a richer data distribution for underrepresented conditions.

3.1.1. Motion-Pathology Disentangled RVQ-VAE

To learn disentangled representations of motion and pathology, we use a Conditional Residual VQ-VAE with two encoders: one for motion and one for pathology.

Encoders. The motion encoder \mathcal{E}_m encodes the input sequence $\mathbf{x} \in \mathbb{R}^{T \times D}$ to a pathology-invariant latent $\mathbf{z}_m = \mathcal{E}_m(\mathbf{x}) \in \mathbb{R}^{T' \times D_m}$ to encode motion dynamics. The pathology encoder, \mathcal{E}_p , is a *conditional* encoder that generates a latent representation from \mathbf{x} , $\mathbf{z}_p = \mathcal{E}_p(\mathbf{x}, c_p) \in \mathbb{R}^{T' \times D_p}$, given the pathology severity level c_p . Conditioning encourages separation between classes in the pathology latent, improving the model’s ability to capture varying degrees of pathology. Here, T' is the downsampled temporal dimensions, and D_m and D_p are the embedding sizes of each latent.

Residual Vector Quantization. We employ Residual Quantization in the motion and pathology encoders to capture hierarchical, discrete features at multiple levels of abstraction. Quantizing the latent space constrains representations to a discrete set of physically plausible poses, which stabilizes training by reducing gradient variance and accelerates convergence. RVQ sequentially quantizes the residuals between the input and outputs of prior quantization layers, enabling the model to capture coarse and fine-grained gait patterns. Let $k \in \{m, p\}$ denote the motion or pathology latent space and $n \in N$ the quantization layer index. The initial latent \mathbf{z}_k is quantized to obtain the first quantized embedding $\mathbf{e}_k^{(0)}$ and codebook indices $\mathbf{h}_k^{(0)}$. Then the residual $\mathbf{r}_k^{(0)}$ is computed by

the error between $\mathbf{e}_k^{(0)}$ and \mathbf{z}_k :

$$\mathbf{e}_k^{(0)} = \text{Quantize}(\mathbf{z}_k), \quad \mathbf{r}_k^{(0)} = \mathbf{z}_k - \mathbf{e}_k^{(0)} \quad (1)$$

For each subsequent layer n , the the previous layer’s residual $\mathbf{r}_k^{(n-1)}$ is quantized to obtain $\mathbf{e}_k^{(n)}$, and a residual $\mathbf{r}_k^{(n)}$:

$$\mathbf{e}_k^{(n)} = \text{Quantize}(\mathbf{r}_k^{(n-1)}) \quad \mathbf{r}_k^{(n)} = \mathbf{r}_k^{(n-1)} - \mathbf{e}_k^{(n)} \quad (2)$$

The final latent representation \mathbf{q}_k for latent k is the sum of all quantized embeddings of the layers: $\mathbf{q}_k = \sum_{n=1}^N \mathbf{e}_k^{(n)}$. This hierarchical structure ensures that both global and local features are effectively captured.

Decoder. Finally, the decoder \mathcal{D} reconstructs the input gait sequence from the combined \mathbf{q}_m and \mathbf{q}_p , $\hat{\mathbf{x}} = \mathcal{D}(\mathbf{q}_m + \alpha \cdot \mathbf{q}_p)$, where α is an interference weight that modulates the level of pathology in the reconstruction.

Training and disentanglement enforcement. To achieve disentanglement, we design the training procedure so that the motion encoder captures only pathology-invariant features, while the pathology encoder isolates pathology-specific information. We first pretrain only the motion encoder \mathcal{E}_m with the decoder \mathcal{D} using reconstruction losses, so that \mathbf{q}_m learns to represent valid motion independently without contributions from the pathology latent. We then train the pathology encoder \mathcal{E}_p and continue fine-tuning \mathcal{E}_m with a reduced learning rate to retain motion content while gradually unlearning pathology-related information. To prevent \mathcal{E}_p from encoding non-pathology information, we constrain its capacity by using fewer codebooks than \mathcal{E}_m . For healthy sequences ($c_p = 0$), we use a latent dropout strategy by zeroing out \mathbf{q}_p during training, forcing \mathcal{E}_m to capture all reconstruction-relevant motion information. With \mathbf{q}_p dropped, reconstruction errors must be corrected solely by the motion latent. The reconstruction loss combines two terms ($\mathcal{L}_{\text{rec}} = \mathcal{L}_{\text{pos}} + \mathcal{L}_{\text{geo}}$). The position loss \mathcal{L}_{pos} is the $L1$ error over non-rotational input components:

$$\mathcal{L}_{\text{pos}} = \|\mathbf{x}_{\text{-rot}} - \hat{\mathbf{x}}_{\text{-rot}}\|_1 \quad (\mathbf{x}_{\text{-rot}} = \mathbf{x} \setminus \mathbf{x}_{\text{rot}}) \quad (3)$$

For rotational components, we compute a geodesic distance loss to ensure rotation comparisons respect the non-Euclidean $\text{SO}(3)$ manifold. First, 6D joint rotations are converted to rotation matrices \mathbf{x}_R using the Gram-Schmidt process [84]. Then the geodesic loss is computed as:

$$\mathcal{L}_{\text{geo}} = \sum^T \arccos \left(\frac{\text{Tr}(\mathbf{x}_R (\hat{\mathbf{x}}_R^{-1})) - 1}{2} \right) \quad (4)$$

To further enforce the disentanglement and prevent information leakage, two auxiliary classifiers are applied to the quantized latents. Each latent is first passed through a self-attention block to aggregate channel information: ($\mathbf{f}_k = \text{SelfAttn}(\mathbf{q}_k)$). A pathology classifier ϕ_p predicts the

severity level from \mathbf{f}_p , while an adversarial pathology classifier ψ_m operates on \mathbf{f}_m , using a gradient reversal layer (GRL) [18], encouraging pathology invariance in the motion latent. The classification (\mathcal{L}_{cls}), adversarial ($\mathcal{L}_{\text{G-adv}}$), and total loss are defined as:

$$\mathcal{L}_{\text{cls}} = \mathbb{E}_{(\mathbf{f}_p, c_p) \sim \mathcal{D}} [\ell_{\text{CE}}(\phi_p(\mathbf{f}_p), c_p)] \quad (5)$$

$$\mathcal{L}_{\text{G-adv}} = \mathbb{E}_{(\mathbf{f}_m, c_p) \sim \mathcal{D}} [\ell_{\text{CE}}(\psi_m(\text{GRL}(\mathbf{f}_m)), c_p)] \quad (6)$$

$$\mathcal{L}_{\text{vq}} = \lambda_r \mathcal{L}_{\text{rec}} + \lambda_c \mathcal{L}_{\text{cls}} + \lambda_{\text{adv}} \mathcal{L}_{\text{adv}} + \lambda_{\text{emb}} \mathcal{L}_{\text{emb}}, \quad (7)$$

with an embedding loss at each quantization layer per latent:

$$\mathcal{L}_{\text{emb}} = \sum_{k \in \{m, p\}} \sum_{n=1}^N \|\mathbf{r}_k^{(n)} - \text{sg}[\mathbf{e}_k^{(n)}]\|_2^2. \quad (8)$$

where $\text{sg}[\cdot]$ denotes the stop-gradient operation. Codebooks are updated using exponential moving averages and codebook reset strategies [81].

3.1.2. Masked Transformer

To generate gait sequences conditioned on pathology, we use a bidirectional Mask Transformer (\mathcal{M}_θ) on the first-layer quantized latents from the disentangled RVQ-VAE. This approach effectively learns VQ-VAE codebook structures and enables fast, high-quality inference generation [23]. Our Mask Transformer is designed to jointly process motion and pathology tokens. A special end-of-motion token, $\langle \text{MEND} \rangle$, is defined to delineate motion and pathology tokens. This structure enables \mathcal{M}_θ to differentiate and selectively attend to motion and pathology tokens [17, 85].

We train \mathcal{M}_θ using a masked token modeling approach inspired by BERT [32]. Tokens from the first quantization layer are concatenated as $\mathbf{h}^{(0)} = [\mathbf{h}_m^{(0)}; \langle \text{MEND} \rangle; \mathbf{h}_p^{(0)}] \in \mathbb{R}^{(2T'+1) \times d}$, with \mathbf{h}_m and \mathbf{h}_p projected to a shared dimension d . A subset of tokens is randomly masked following a cosine noise schedule $\beta(t)$, and the model predicts the masked tokens by minimizing a cross-entropy loss ($\mathcal{L}_{\text{mTrans}}$) where \tilde{m} represents the set of masked token indices and $\tilde{\mathbf{h}}$ is the masked sequence.

$$\mathcal{L}_{\text{mTrans}} = - \sum_{i \in \tilde{m}} \log \mathcal{M}_\theta(\mathbf{h}_i^{(0)} \mid \tilde{\mathbf{h}}, c_p) \quad (9)$$

During inference, \mathcal{M}_θ starts from a fully masked sequence and iteratively predicts base-layer’s masked tokens conditioned on c_p . At each step, it selects high-confidence tokens, re-masks low-confidence ones, and continues this refinement over R steps.

3.1.3. Residual Transformer

A single bidirectional residual transformer (\mathcal{R}_θ) is used to generate residuals in the RVQ-VAE via a next layer tokens prediction strategy. At each quantization layer n , \mathcal{R}_θ predicts current residuals from the cumulative embedded tokens

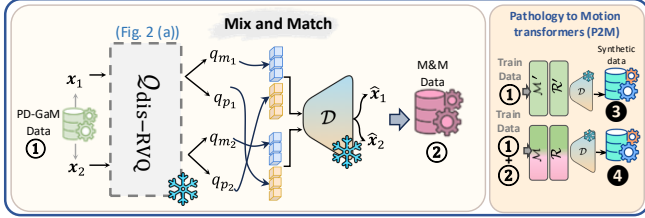


Figure 3. Mix and Match augmentation. Motion latent codes (q_m) from one sample are combined with pathology latent codes (q_p) from another to synthesize new gait sequences.

$\mathbf{h}_k^{(0:n-1)}$, conditioned on severity c_p and layer index n , refining fine-grained details progressively. Each quantization layer uses separate motion and pathology embeddings. Following [23], parameter sharing is applied between successive layer embeddings within each token type to improve training efficiency while preserving the semantic distinction between motion and pathology tokens. The residual transformer minimizes the cross-entropy loss at each layer n :

$$\mathcal{L}_{\text{res}} = - \sum_{n=1}^N \sum_{\substack{i=1 \\ \mathbf{h}_i \neq \langle \text{MEND} \rangle}}^{2T'+1} \log \mathcal{R}_\theta(\mathbf{h}_{k,i}^{(n)} | \mathbf{h}_k^{(0:n-1)}, c_p, n), \quad (10)$$

During training, n is sampled randomly. At inference, \mathcal{R}_θ starts from \mathcal{M}_θ 's output and sequentially predicts residual tokens, and updates the cumulative embedding over n steps. The final cumulative embedding is passed to the pretrained decoder to reconstruct the gait sequence. Since motion and pathology use separate codebooks, both transformers use distinct output heads for their token predictions.

Motion-Pathology Mix and Match Augmentation. Our disentangled latent space enables a novel Mix and Match augmentation (M&M) strategy that combines motion features from one sample with pathology features from another to synthesize new gait sequences, akin to latent mixing (Fig. 3). This allows applying the pathology profile of one sample to the motion dynamics of another. Given the scarcity of severe pathology cases in PD datasets, we use this method to augment the severe class, increasing diversity and improving our generative model training.

4. Experiments

4.1. Datasets and Evaluation Metrics

Dataset. We introduce PD-GaM, a fully anonymized and publicly available dataset derived from PD4T [11]. Unlike PD4T videos, which require ethics approval and request procedures, PD-GaM is openly accessible. It includes 1701 gait sequences from 30 individuals with PD, each labeled by an expert with UPDRS-gait scores ranging from 0 to 3 (participants with a score of 4 are typically unable to walk without substantial assistance). Videos are segmented to isolate gait segments, and SMPL parameters [40] are extracted using WHAM [65] (see supplement for clinical validity), followed

| Method | AVE ↓ | AAMD ↓ | ASMD ↓ | Div → |
|----------------------------|--------------|--------------|--------------|--------------|
| Real | - | - | - | 3.894 |
| StableMoFusion* [28] | 1.437 | 1.568 | 0.201 | 2.774 |
| MMM* [53] | 1.037 | 0.791 | 0.118 | 2.421 |
| SnapMoGen* [24] | 0.745 | 0.526 | 0.166 | 2.372 |
| MoMask* [23] | 0.898 | 0.440 | 0.106 | 2.516 |
| GAITGen _{w/o-dis} | 0.569 | 0.222 | 0.076 | 2.475 |
| GAITGen | 0.194 | 0.096 | 0.048 | 3.966 |

Table 1. Comparison of GAITGen with baselines on the pathology-conditioned motion generation task. “*” denotes baseline trained on PD-GaM. “→” the closer to real the better.

| Method | Gen. train | Cls. train/test | F1 ↑ | prec. ↑ | rec. ↑ |
|--------------------------------------|------------|-----------------|-------------|-------------|-------------|
| w/o synthetic data | - | ①/① | 0.66 | 0.66 | 0.65 |
| + ⑤ MoMask* synthetic | ① | ⑤+①/① | 0.51 | 0.59 | 0.49 |
| + ⑥ MoMask [†] synthetic | ①+② | ⑥+①/① | 0.57 | 0.60 | 0.53 |
| + ② GAITGen (M&M Only) synthetic | - | ②+①/① | 0.69 | 0.67 | 0.70 |
| + ③ GAITGen (P2M - No M&M) synthetic | ① | ③+①/① | 0.71 | 0.70 | 0.71 |
| + ④ GAITGen (Full P2M) synthetic | ①+② | ④+①/① | 0.74 | 0.76 | 0.73 |

Table 2. The effect of synthetic data on downstream UPDRS-gait classification. *Gen.* → Generative model, *Cls.* → Classifier, M&M → Mix and Match, P2M → Pathology to Motion. “*” and “†” indicate the model is retrained on the specified data. (see Fig. 3 for numbered data types.)

by post-processing to correct global trajectory artifacts introduced during mesh estimation. Dataset splits are participant-wise to ensure unbiased evaluation (see supplement). As of today, PD-GaM is the largest public dataset with UPDRS 3 gaits, critical for addressing severe-case scarcity and central to our motivation. Cross-dataset evaluations on T-SDU-PD [59] and BMCLab [64] test GAITGen’s generalization beyond PD-GaM.

Metrics. Conventional metrics, such as FID, are unsuitable here due to limited data diversity and class imbalance, particularly for severe cases. FID requires large, diverse samples to reliably estimate distribution statistics [10], which PD datasets lack. Instead, we employ clinically-relevant metrics to assess (1) generation quality, (2) representation learning, and (3) reconstruction fidelity.

(1) Average Variance Error (AVE) [19, 52] measures variance between generated and Ground Truth (GT) joints movements, evaluating class-wise variability in joint velocities. Absolute Arm-swing Mean Difference (AAMD) quantifies variance between generated and GT arm-swing. Lower AAMD indicates that generated sequences closely match the GT variance, accurately reflecting pathology-specific arm motion reduction typical in PD [30, 45]. Absolute Stooped Posture Mean Difference (ASMD) measures variance in torso inclination, capturing the stooped posture commonly observed in severe PD [30]. Diversity (Div), following [22], assesses intra-class variability, measuring the diversity of generated gaits in each severity level.

(2) Pathology-Only Reconstruction Error (PORE) quantifies the extent of motion information leakage into the pathol-

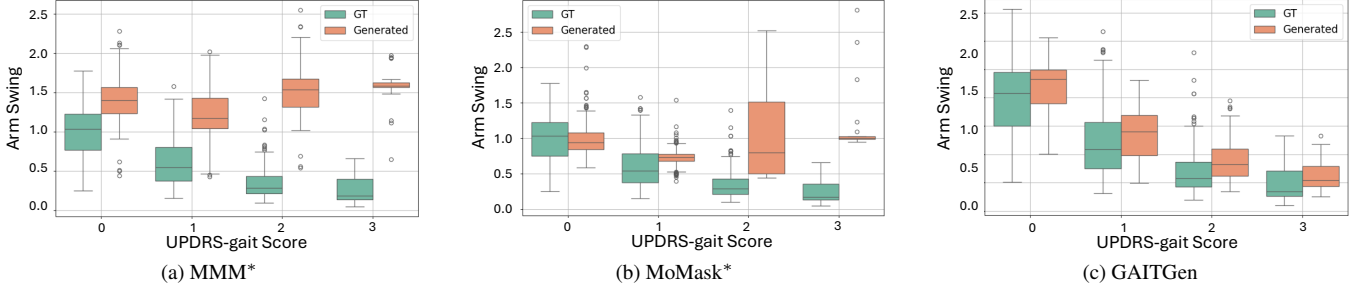


Figure 4. Comparison of arm-swing variability across MDS-UPDRS scores for GT and synthetic sequences.

ogy latent by comparing the Mean Per Joint Position Error (MPJPE) under two conditions: 1) reconstruction using only the pathology latent \mathbf{q}_p (denoted e_p), 2) reconstruction using both latents $\mathbf{q}_m + \mathbf{q}_p$ (denoted e_{pm}). Higher e_p and lower e_{pm} is preferred. The metric is defined as:

$$\text{PORE} = \frac{e_p - e_{pm}}{e_{pm} + \epsilon} \quad (11)$$

A higher PORE reflects better disentanglement with minimal motion information leakage into the pathology space. Pathology-Motion Predictive Gap (**PMPG**) assesses latent spaces separation by measuring the difference between PD classification accuracy from each pathology (\mathbf{q}_p) and motion (\mathbf{q}_m) latent codes. A high PMPG indicates that pathology information is well captured in \mathbf{q}_p with minimal leakage into \mathbf{q}_m . Disentanglement Score (**DS**) provides a combined measure of the separation, calculated as the geometric mean of PORE and PMPG. A higher DS indicates stronger disentanglement, with minimal information leakage and effective encoding of pathological characteristics.

(3) Similar to [9], we use **MPJPE** and **PA-MPJPE** (Procrustes Aligned) to assess global and local reconstruction errors, and Acceleration Error (**ACCL**) for temporal quality.

4.2. Baseline Comparison

As no existing baseline addresses pathology-conditioned gait generation, we establish new baselines by adapting state-of-the-art motion generation models, MoMask [23], MMM [53], StableMoFusion [28] and SnapMoGen [24], retraining them on our PD-GaM dataset for this task. 13k gait sequences are generated uniformly across 4 severity levels from each model. GAITGen consistently outperforms both baselines across all metrics (Tab. 1). Comparing GAITGen with a non-disentangled version of it (GAITGen_{w/o-dis}), which is trained only with one conditional encoder without the \mathcal{L}_{cls} and \mathcal{L}_{G-adv} , underscores the necessity of disentanglement for capturing subtle, pathology-specific features. Fig. 4 illustrates arm-swing distributions across severity levels for each method, showing that GAITGen closely matches ground truth patterns and reflects the reduction in arm-swing at higher severity levels, a result not achieved by the baseline models.

| | ConvAutoEnc [22] | PoseFormerV2 [2, 83] | ST-GCN PD [59] | GaitFeatures+RF |
|----------------------|--------------------|----------------------|----------------|-----------------|
| F ₁ score | 0.66 → 0.74 | 0.62 → 0.69 | 0.40 → 0.49 | 0.39 → 0.44 |
| | (+8 pp) | (+7 pp) | (+9 pp) | (+5 pp) |

Table 3. Performance gains across PD classifiers on real data.

4.3. Downstream Task

To assess the utility of GAITGen synthetic data, we examine its effect on a downstream UPDRS-gait classification task. Tab. 2 compares performance with various training sources and tested on PD-GaM test set: a) with no synthetic data, and then augmented with b) MoMask* synthetic data ⑤ (when trained on only PD-GaM ①), c) MoMask† synthetic data ⑥ (when trained on ① + GAITGen M&M data ②), d) only GAITGen M&M data ②, e) GAITGen synthetic data ③ (when trained on ①) f) GAITGen synthetic data ④ (when trained on ①+②). For M&M, we created 300 samples combining z_m from gait sequences with a UPDRS-gait score of 1 with z_p from gaits with a score of 3 in the PD-GaM dataset (Fig. 3), augmenting the underrepresented class 3. From each variant of MoMask and GAITGen (black circled numbers), trained on different data, we generated 1000 synthetic samples, 400 for class 3 and 200 for others to mitigate class imbalance. Adding M&M improves results across configurations. Inclusion of GAITGen final synthetic data achieves the best result across all metrics, while MoMask results in reduced performance.

4.3.1. Cross-Classifer Validation

Extending beyond the single-classifier evaluation, we assess the effect of GAITGen data across four downstream models: *frozen* pre-trained backbones are a convolutional encoder from established motion generation benchmarks [9, 23, 69], a transformer-based model (PoseFormerV2) which is the best classifier from previous PD benchmark [2, 83], a PD-specific ST-GCN [59], all with a lightweight *trainable* MLP classifier heads and a Random Forest trained on hand-crafted gait features derived from generated sequences, proven to distinguish PD from control [47]. As shown in Tab. 3, all classifiers' F₁ score improved with synthetic augmentation. The consistent performance gains suggest GAITGen contributes generalizable gait patterns beneficial to varied PD classifiers (see supplement for details).

| Exp. | Train Data | Test Data | Inc. Severe (labels) | F ₁ | prec. | rec. |
|------|-----------------------------|-----------|----------------------|----------------|-------------|-------------|
| IDE | PD-GaM (<i>no-syn</i>) | PD-GaM | ✓ (0,1,2,3) | 0.66 | 0.66 | 0.65 |
| IDE | PD-GaM + GAITGen | PD-GaM | ✓ (0,1,2,3) | 0.74 | 0.76 | 0.73 |
| IDE | T-SDU-PD (<i>no-syn</i>) | T-SDU-PD | × (0,1,2) | 0.49 | 0.51 | 0.49 |
| EV | PD-GaM (<i>no-syn</i>) | T-SDU-PD | × (0,1,2) | 0.44 | 0.47 | 0.47 |
| EV | PD-GaM + GAITGen | T-SDU-PD | × (0,1,2) | 0.53 | 0.55 | 0.52 |
| IDE | T-SDU-PD + GAITGen | T-SDU-PD | × (0,1,2) | <u>0.57</u> | <u>0.56</u> | <u>0.58</u> |
| TAA | PD-GaM + T-SDU-PD + GAITGen | T-SDU-PD | × (0,1,2) | 0.60 | 0.58 | 0.61 |
| IDE | BMClab (<i>no-syn</i>) | BMClab | × (0,1,2) | 0.57 | 0.59 | 0.56 |
| EV | PD-GaM (<i>no-syn</i>) | BMClab | × (0,1,2) | 0.52 | 0.54 | 0.52 |
| EV | PD-GaM + GAITGen | BMClab | × (0,1,2) | 0.62 | 0.65 | 0.61 |
| IDE | BMClab + GAITGen | BMClab | × (0,1,2) | <u>0.69</u> | <u>0.70</u> | <u>0.70</u> |
| TAA | PD-GaM + BMClab + GAITGen | BMClab | × (0,1,2) | 0.71 | 0.74 | 0.72 |

Table 4. Cross-dataset evaluation. In Domain Evaluation (IDE), External Validation (EV), Target-aware Adaptation (TAA). The best results per dataset are bold, and second-best are underlined.

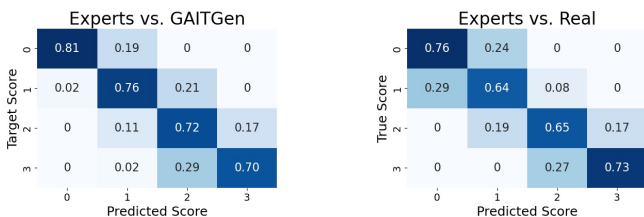


Figure 5. User study comparing experts (n=6) scoring of gait sequences with the true labels. True scores indicate (Left)-synthetic subset: condition given to GAITGen for generation, (Right) Real subset: UPDRS-gait score provided by the PD-GaM dataset.

4.3.2. Cross-dataset Evaluation

To assess the generalizability of GAITGen beyond PD-GaM, we evaluated its impact on two independent datasets: T-SDU-PD [59] and BMClab [64]. Results in Tab. 4 show consistent improvements across three evaluation settings. In the in-domain evaluation (IDE), adding GAITGen samples to the training set improves performance relative to training only on real data, e.g., F₁ scores improve +8 pp on T-SDU-PD and +12 pp on BMClab. In the external validation (EV), training on PD-GaM and testing on the other datasets, GAITGen augmentation raises F₁ by +9 pp on T-SDU-PD and +10 pp on BMClab. Finally, in the target-aware adaptation (TAA), combining real and GAITGen synthetic data across domains yields the best performance overall, achieving F₁ of 0.60 on T-SDU-PD and 0.71 on BMClab. These consistent gains confirm that GAITGen contributes transferable pathological gait patterns that improve severity estimation beyond the source dataset. Compared to prior SOTA, GAITGen achieves markedly higher F₁ scores (0.60 vs. 0.38 from ST-GCN PD [59] on T-SDU-PD; 0.71 vs. 0.58 from AGIR [71] on BMClab), demonstrating superior performance on both datasets.

4.4. Clinical User Study

To evaluate the clinical relevance of GAITGen synthetic gait sequences, we conducted a user study involving six PD experts with extensive experience of UPDRS assessment

| Name | AuxCIS | Comb. | \mathcal{L}_{rec} | H _p Mask | Pretrain | #cb _m , #cb _p |
|------------------------------|------------------|-------|---------------------|---------------------|----------|-------------------------------------|
| 1CLS | ϕ_p | conc | ℓ_1 | ✗ | ✗ | 512,512 |
| 2CLS | ϕ_p, ψ_m | conc | ℓ_1 | ✗ | ✗ | 512,512 |
| AdaStyle | ϕ_p, ψ_m | AdaLN | ℓ_1 | ✗ | ✗ | 512,512 |
| 2CLS-cb _p (128) | ϕ_p, ψ_m | conc | ℓ_1 | ✗ | ✗ | 512,128 |
| GeoL1 | ϕ_p, ψ_m | conc | Geo+ ℓ_1 | ✗ | ✗ | 512,128 |
| ADD | ϕ_p, ψ_m | add | Geo+ ℓ_1 | ✗ | ✗ | 512,128 |
| ADD- $\mathcal{H}_{dropout}$ | ϕ_p, ψ_m | add | Geo+ ℓ_1 | dropout | ✗ | 512,128 |
| ADD- $\mathcal{H}_{zeroout}$ | ϕ_p, ψ_m | add | Geo+ ℓ_1 | zeroed | ✗ | 512,128 |
| GAITGen | ϕ_p, ψ_m | add | Geo+ ℓ_1 | ✓ | ✓ | 512,128 |

| Method | Reconstruction | | | | Generation |
|------------------------------|----------------|--------------|--------------|-------------|-------------|
| | MPJPE ↓ | PAMPJPE ↓ | ACCL ↓ | DS ↑ | AVE ↓ |
| 1CLS | 67.31 | 34.23 | 17.63 | 0.22 | 1.37 |
| 2CLS | 92.29 | 59.06 | 30.51 | 0.34 | 1.45 |
| AdaStyle | 96.16 | 62.88 | 32.02 | 0.21 | 1.98 |
| 2CLS-cb _p (128) | 103.50 | 72.61 | 34.40 | 0.80 | 1.47 |
| GeoL1 | 80.12 | 49.13 | 30.14 | 0.82 | 0.91 |
| ADD | 80.11 | 48.77 | 29.34 | 0.81 | 0.90 |
| ADD- $\mathcal{H}_{dropout}$ | 75.67 | 39.23 | 24.97 | 0.83 | 0.81 |
| ADD- $\mathcal{H}_{zeroout}$ | 69.15 | 30.42 | 18.55 | 0.83 | 0.74 |
| $\mathcal{E}_p - w/o C_p$ | 31.04 | 18.32 | 19.95 | 0.81 | 0.34 |
| w/o RQ | 58.42 | 26.11 | 25.07 | 0.77 | 0.62 |
| GAITGen | 28.38 | 17.91 | 15.35 | 1.21 | 0.19 |

Table 5. Ablation for both reconstruction and generation tasks.

(four specialist physicians and two research fellows), following standard expert-review protocols in medical AI studies [16, 34, 42, 56, 67]. The raters were presented with 65 randomly selected video samples (34 real, 31 synthetic). They were tasked with: (1) classifying each video as either real or synthetic, (2) assigning a UPDRS-gait score (ranging from 0 to 3) to each video. Results for each task were averaged across the all raters. The precision and recall for the first task were both 0.52 (near chance performance), indicating that GAITGen’s outputs are visually realistic and challenging to distinguish from real data.

Fig. 5–left compares clinician-assigned UPDRS-gait scores with that of the pathology condition provided to GAITGen during generation. The near diagonal confusion matrix highlights GAITGen’s effectiveness in matching the condition. Fig. 5–right compares clinician scores with the PD-GaM UPDRS-gait scores, also showing strong alignment and the differences are attributable to the somewhat subjective nature of the assessment. The inter-rater agreement was measured using Weighted Kappa and Intraclass Correlation Coefficient (ICC). The Kappa value of 0.93 and ICC of 0.93 (95% CI [0.88, 0.94]) indicate almost perfect agreement between the raters, with average raters-ground truth agreement at 0.91 (SD = 0.03). Notably, raters showed higher agreement on the synthetic subset compared to the real subset (ICC 0.93 vs. 0.86). These results match the reliability ranges reported in prior research for UPDRS-gait [13, 57], supporting GAITGen’s clinical validity.

4.5. Ablation Studies

Ablation studies are conducted incrementally, adding one component at a time to evaluate the contributions of each component (Tab. 5). **Classifier Trade-offs.** Using a single classifier on the pathology latent (1CLS) results in moderate

(a) Synthetic Score 0 (b) Synthetic Score 1 (c) Synthetic Score 2 (d) Synthetic Score 3

Figure 6. Synthetic gait animations generated by GAITGen. (Best viewed with Acrobat Reader. Click the images to play the animations.)

(a) Real Score 1 (b) Real Score 3 (c) Mix and Match

Figure 7. (a) and (b) are two real samples from PD-GaM dataset with UPDRS-gait scores 1 and 3. Mix and Match sequence in (c) takes motion from (a) and pathology from (b). (Best viewed with Acrobat Reader. Click the images to play the animation clips.)

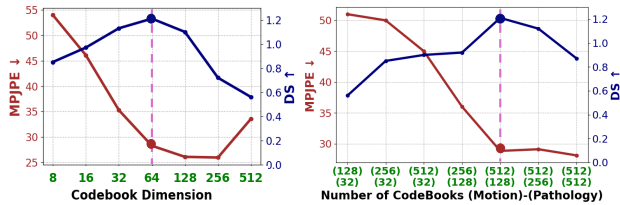


Figure 8. Evaluation of MPJPE and DS across various codebook dimensions and motion-pathology codebook sizes.

reconstruction performance but a low disentanglement score (DS) due to motion information leakage into the pathology latent. Introducing an adversarial classifier on the motion latent (2CLS) improves the DS, however, reconstruction errors increase, indicating a trade-off when relying solely on classification losses. Similarly, reducing the codebook size of the pathology (2CLS- $cb_p(128)$) enhances the DS by limiting its capacity to encode motion information. Expectedly, this adjustment increases reconstruction errors.

H_p Latent Dropout. To improve reconstruction, we mask the pathology latent for healthy samples using deterministic zeroing (ADD- $\mathcal{H}_{zeroout}$) and stochastic dropout (ADD- $\mathcal{H}_{dropout}$, $p = 0.5$), encouraging to fully capture healthy gait dynamics. Both enhance DS slightly and reduce reconstruction errors notably, with zeroing showing greater gains by ensuring that the motion encoder focuses on motion-related features without relying on the pathology latent. When combined with motion-encoder pretraining, this yields the best performance across all metrics (GAITGen).

Pathology as Style. Treating pathology as style via adaptive layer normalization (AdaStyle) increases reconstruction errors and lowers DS. This confirms that modeling pathology as a style conflates motion and pathology features, making

it challenging to control and synthesize gait sequences with specific pathology, especially for severe cases.

Rotation-Aware Loss. Geodesic loss (GeoL1) significantly improves reconstruction, underscoring the importance of respecting the non-Euclidean nature of rotations in $SO(3)$, as Euclidean distances can lead to incorrect gradients.

Conditioning & Residual Quantization. Using an unconditional pathology encoder (\mathcal{E}_p w/o C_p) decreases the DS and increases reconstruction errors. Conditioning pushes apart classes in the pathology latent, enhancing separability between different severity levels. Finally, omitting Residual Vector Quantization (w/o RQ) degrades performance, confirming the importance of hierarchical quantization in capturing multi-level motion features.

Codebook ablation. Fig. 8 presents the MPJPE and DS across different codebook dimensions and motion-pathology codebook sizes. Best setting is selected to balance high DS with low MPJPE, optimizing both disentanglement and reconstruction accuracy.

4.6. Qualitative Results

Fig. 6 shows synthetic sequences generated by GAITGen for each severity level. Fig. 7 presents a M&M augmentation result, where motion features, such as curved walk in a gait with UPDRS score 1 (a) are combined with pathology features of a gait with score 3 (b), resulting in a more stooped posture, reduced arm swing, and shorter strides in (c). Unlike style transfer methods, this augmentation reflects severity-related constraints (e.g., shorter traversable distances typical of severe gait impairment for UPDRS-gait score 3). The balance between motion and pathology is adjustable via the interference weight α . Details in the Supplement.

5. Conclusion

We proposed GAITGen, a novel model for generating clinically relevant gait sequences conditioned on pathology severity by disentangling motion dynamics from pathology-specific factors. Alongside GAITGen, we introduced PD-GaM, the largest 3D mesh Parkinsonian gait dataset, supporting clinical gait research. While our approach shows promise in capturing key features of parkinsonian gait and mitigating data scarcity, there remains significant potential for further exploration. Future work could integrate additional clinically relevant inputs, such as textual descriptions, by leveraging foundation models for supervision to enhance the richness of the generated data. Additionally, extending the model to include other manifestations of PD, such as tremors or dyskinesias, would provide a more comprehensive representation of the condition. These directions broaden GAITGen’s potential integration into clinical practice, contributing to the development of tools for better diagnosis, monitoring, and treatment planning for movement disorders.

Acknowledgement. This work was supported in part by the Vector Institute for Artificial Intelligence and KITE – Toronto Rehabilitation Institute – University Health Network. Additional support was provided by the Data Sciences Institute at the University of Toronto, the Walter and Maria Schroeder Institute for Brain Innovation and Recovery, the Canadian Institutes of Health Research (CIHR), and the AMS Healthcare Fellowship in Compassion and Artificial Intelligence. The authors sincerely thank these institutions for their support.

References

- [1] Kfir Aberman, Yijia Weng, Dani Lischinski, Daniel Cohen-Or, and Baoquan Chen. Unpaired motion style transfer from video to animation. *ACM Transactions on Graphics (TOG)*, 39(4): 64–1, 2020. 2
- [2] Vida Adeli, Soroush Mehraban, Irene Ballester, Yasamin Zarghami, Andrea Sabo, Andrea Iaboni, and Babak Taati. Benchmarking skeleton-based motion encoder models for clinical applications: Estimating parkinson’s disease severity in walking sequences. In *2024 IEEE 18th International Conference on Automatic Face and Gesture Recognition (FG)*, pages 1–10. IEEE, 2024. 1, 6
- [3] Andrea Avogaro, Federico Cunico, Bodo Rosenhahn, and Francesco Setti. Markerless human pose estimation for biomedical applications: a survey. *Frontiers in Computer Science*, 5:1153160, 2023. 1
- [4] Sagie Benaim, Michael Khaitov, Tomer Galanti, and Lior Wolf. Domain intersection and domain difference. In *Proceedings of the IEEE/CVF International Conference on Computer Vision*, pages 3445–3453, 2019. 2
- [5] Aurélie Bertaux, Mathieu Gueugnon, Florent Moissenet, Baptiste Orliac, Pierre Martz, Jean-François Maillefert, Paul Ornetti, and Davy Laroche. Gait analysis dataset of healthy volunteers and patients before and 6 months after total hip arthroplasty. *Scientific Data*, 9(1):399, 2022. 4
- [6] José Carrasco-Plaza and Mauricio Cerda. Evaluation of human pose estimation in 3d with monocular camera for clinical application. In *International Symposium on Intelligent Computing Systems*, pages 121–134. Springer, 2022. 1
- [7] Ziyi Chang, Edmund JC Findlay, Haozheng Zhang, and Hubert PH Shum. Unifying human motion synthesis and style transfer with denoising diffusion probabilistic models. *arXiv preprint arXiv:2212.08526*, 2022. 2
- [8] Jorge Marquez Chavez and Wei Tang. A vision-based system for stage classification of parkinsonian gait using machine learning and synthetic data. *Sensors*, 22(12):4463, 2022. 2
- [9] Xin Chen, Biao Jiang, Wen Liu, Zilong Huang, Bin Fu, Tao Chen, and Gang Yu. Executing your commands via motion diffusion in latent space. In *Proceedings of the IEEE/CVF Conference on Computer Vision and Pattern Recognition*, pages 18000–18010, 2023. 2, 6
- [10] Min Jin Chong and David Forsyth. Effectively unbiased fid and inception score and where to find them. In *Proceedings of the IEEE/CVF conference on computer vision and pattern recognition*, pages 6070–6079, 2020. 5
- [11] Amirhossein Dadashzadeh, Shuchao Duan, Alan Whone, and Majid Mirmehdi. PeCop: Parameter efficient continual pre-training for action quality assessment. In *Proceedings of the IEEE/CVF Winter Conference on Applications of Computer Vision*, pages 42–52, 2024. 1, 5
- [12] Wenxun Dai, Ling-Hao Chen, Jingbo Wang, Jinpeng Liu, Bo Dai, and Yansong Tang. MotionLCM: Real-time controllable motion generation via latent consistency model. *arXiv preprint arXiv:2404.19759*, 2024. 2
- [13] T de Deus Fonticoba, D Santos García, and M Macías Arribí. Inter-rater variability in motor function assessment in parkinson’s disease between experts in movement disorders and nurses specialising in pd management. *Neurología (English Edition)*, 34(8):520–526, 2019. 1, 7
- [14] Aaron Defazio, Xingyu Alice Yang, Harsh Mehta, Konstantin Mishchenko, Ahmed Khaled, and Ashok Cutkosky. The road less scheduled. *arXiv preprint arXiv:2405.15682*, 2024. 4
- [15] Daniel Deng, Jill L Ostrem, Vy Nguyen, Daniel D Cummins, Julia Sun, Anupam Pathak, Simon Little, and Reza Abbasi-Asl. Interpretable video-based tracking and quantification of parkinsonism clinical motor states. *npj Parkinson’s Disease*, 10(1):122, 2024. 1
- [16] Zhaojie Fang, Zhanghao Chen, Pengxue Wei, Wangting Li, Shaochong Zhang, Ahmed Elazab, Gangyong Jia, Ruiquan Ge, and Changmiao Wang. Uwat-gan: Fundus fluorescein angiography synthesis via ultra-wide-angle transformation multi-scale gan. In *International conference on medical image computing and computer-assisted intervention*, pages 745–755. Springer, 2023. 7
- [17] Yao Feng, Jing Lin, Sai Kumar Dwivedi, Yu Sun, Priyanka Patel, and Michael J Black. ChatPose: Chatting about 3d human pose. In *Proceedings of the IEEE/CVF Conference on Computer Vision and Pattern Recognition*, pages 2093–2103, 2024. 4
- [18] Yaroslav Ganin and Victor Lempitsky. Unsupervised domain adaptation by backpropagation. In *International conference on machine learning*, pages 1180–1189. PMLR, 2015. 4

- [19] Anindita Ghosh, Noshaba Cheema, Cennet Oguz, Christian Theobalt, and Philipp Slusallek. Synthesis of compositional animations from textual descriptions. In *Proceedings of the IEEE/CVF international conference on computer vision*, pages 1396–1406, 2021. 5
- [20] Christopher G Goetz, Barbara C Tilley, Stephanie R Shaftman, Glenn T Stebbins, Stanley Fahn, Pablo Martinez-Martin, Werner Poewe, Cristina Sampaio, Matthew B Stern, Richard Dodel, et al. Movement disorder society-sponsored revision of the unified parkinson’s disease rating scale (MDS-UPDRS): scale presentation and clinimetric testing results. *Movement disorders: official journal of the Movement Disorder Society*, 23(15):2129–2170, 2008. 1
- [21] Gautier Grouvel, Lena Carcreff, Florent Moissenet, and Stéphane Armand. A dataset of asymptomatic human gait and movements obtained from markers, imus, insoles and force plates. *Scientific Data*, 10(1):180, 2023. 4
- [22] Chuan Guo, Shihao Zou, Xinxin Zuo, Sen Wang, Wei Ji, Xingyu Li, and Li Cheng. Generating diverse and natural 3d human motions from text. In *Proceedings of the IEEE/CVF Conference on Computer Vision and Pattern Recognition*, pages 5152–5161, 2022. 2, 5, 6
- [23] Chuan Guo, Yuxuan Mu, Muhammad Gohar Javed, Sen Wang, and Li Cheng. MoMask: Generative masked modeling of 3d human motions. In *Proceedings of the IEEE/CVF Conference on Computer Vision and Pattern Recognition*, pages 1900–1910, 2024. 2, 4, 5, 6
- [24] Chuan Guo, Inwoo Hwang, Jian Wang, and Bing Zhou. Snapmogen: Human motion generation from expressive texts. *arXiv preprint arXiv:2507.09122*, 2025. 5, 6
- [25] Irina Higgins, Loic Matthey, Arka Pal, Christopher P Burgess, Xavier Glorot, Matthew M Botvinick, Shakir Mohamed, and Alexander Lerchner. beta-VAE: Learning basic visual concepts with a constrained variational framework. *ICLR (Poster)*, 3, 2017. 2
- [26] Ting-Yao Hu, Mohammadreza Armandpour, Ashish Shrivastava, Jen-Hao Rick Chang, Hema Koppula, and Oncel Tuzel. SYNT++: Utilizing imperfect synthetic data to improve speech recognition. In *ICASSP 2022-2022 IEEE International Conference on Acoustics, Speech and Signal Processing (ICASSP)*, pages 7682–7686. IEEE, 2022. 2
- [27] Siteng Huang, Biao Gong, Yutong Feng, Xi Chen, Yuqian Fu, Yu Liu, and Donglin Wang. Learning disentangled identifiers for action-customized text-to-image generation. In *Proceedings of the IEEE/CVF Conference on Computer Vision and Pattern Recognition*, pages 7797–7806, 2024. 2
- [28] Yiheng Huang, Hui Yang, Chuanchen Luo, Yuxi Wang, Shibo Xu, Zhaoxiang Zhang, Man Zhang, and Junran Peng. Stablemofusion: Towards robust and efficient diffusion-based motion generation framework. In *Proceedings of the 32nd ACM International Conference on Multimedia*, pages 224–232, 2024. 5, 6
- [29] Khawar Islam, Muhammad Zaigham Zaheer, Arif Mahmood, and Karthik Nandakumar. DiffuseMix: Label-preserving data augmentation with diffusion models. In *Proceedings of the IEEE/CVF Conference on Computer Vision and Pattern Recognition*, pages 27621–27630, 2024. 2
- [30] Joseph Jankovic. Parkinson’s disease: clinical features and diagnosis. *Journal of neurology, neurosurgery & psychiatry*, 79(4):368–376, 2008. 1, 5, 2
- [31] Hanbyul Joo, Hao Liu, Lei Tan, Lin Gui, Bart Nabbe, Iain Matthews, Takeo Kanade, Shohei Nobuhara, and Yaser Sheikh. Panoptic studio: A massively multiview system for social motion capture. In *Proceedings of the IEEE international conference on computer vision*, pages 3334–3342, 2015. 1
- [32] Jacob Devlin Ming-Wei Chang Kenton and Lee Kristina Toutanova. BERT: Pre-training of deep bidirectional transformers for language understanding. In *Proceedings of naacL-HLT*, page 2. Minneapolis, Minnesota, 2019. 4
- [33] Kyungdo Kim, Sihan Lyu, Sneha Mantri, and Timothy W Dunn. TULIP: Multi-camera 3d precision assessment of parkinson’s disease. In *Proceedings of the IEEE/CVF Conference on Computer Vision and Pattern Recognition*, pages 22551–22562, 2024. 1
- [34] Oran Lang, Doron Yaya-Stupp, Ilana Traynis, Heather Cole-Lewis, Chloe R Bennett, Courtney R Lyles, Charles Lau, Michal Irani, Christopher Semturs, Dale R Webster, et al. Using generative ai to investigate medical imagery models and datasets. *EBioMedicine*, 102, 2024. 7
- [35] Doyup Lee, Chiheon Kim, Saehoon Kim, Minsu Cho, and Wook-Shin Han. Autoregressive image generation using residual quantization. In *Proceedings of the IEEE/CVF conference on computer vision and pattern recognition*, pages 11523–11532, 2022. 3
- [36] Renshuai Liu, Bowen Ma, Wei Zhang, Zhipeng Hu, Changjie Fan, Tangjie Lv, Yu Ding, and Xuan Cheng. Towards a simultaneous and granular identity-expression control in personalized face generation. In *Proceedings of the IEEE/CVF Conference on Computer Vision and Pattern Recognition*, pages 2114–2123, 2024. 2
- [37] Francesco Locatello, Gabriele Abbati, Thomas Rainforth, Stefan Bauer, Bernhard Schölkopf, and Olivier Bachem. On the fairness of disentangled representations. *Advances in neural information processing systems*, 32, 2019. 2
- [38] Francesco Locatello, Stefan Bauer, Mario Lucic, Gunnar Raetsch, Sylvain Gelly, Bernhard Schölkopf, and Olivier Bachem. Challenging common assumptions in the unsupervised learning of disentangled representations. In *international conference on machine learning*, pages 4114–4124. PMLR, 2019. 2
- [39] Francesco Locatello, Michael Tschannen, Stefan Bauer, Gunnar Rätsch, Bernhard Schölkopf, and Olivier Bachem. Disentangling factors of variation using few labels. *arXiv preprint arXiv:1905.01258*, 2019. 2
- [40] Matthew Loper, Naureen Mahmood, Javier Romero, Gerard Pons-Moll, and Michael J. Black. SMPL: A skinned multi-person linear model. *ACM Trans. Graphics (Proc. SIGGRAPH Asia)*, 34(6):248:1–248:16, 2015. 5
- [41] Mandy Lu, Kathleen Poston, Adolf Pfefferbaum, Edith V Sullivan, Li Fei-Fei, Kilian M Pohl, Juan Carlos Niebles, and Ehsan Adeli. Vision-based estimation of MDS-UPDRS gait scores for assessing parkinson’s disease motor severity. In *Medical Image Computing and Computer Assisted Intervention—MICCAI 2020: 23rd International Conference, Lima, Peru, October 4–8, 2020, Proceedings, Part III 23*, pages 637–647. Springer, 2020. 1

- [42] Mandy Lu, Qingyu Zhao, Kathleen L Poston, Edith V Sullivan, Adolf Pfefferbaum, Marian Shahid, Maya Katz, Leila Montaser Kouhsari, Kevin Schulman, Arnold Milstein, et al. Quantifying parkinson’s disease motor severity under uncertainty using MDS-UPDRS videos. *Medical image analysis*, 73: 102179, 2021. 1, 7
- [43] Naureen Mahmood, Nima Ghorbani, Nikolaus F Troje, Gerard Pons-Moll, and Michael J Black. Amass: Archive of motion capture as surface shapes. In *Proceedings of the IEEE/CVF international conference on computer vision*, pages 5442–5451, 2019. 6
- [44] Sina Mehdizadeh, Hoda Nabavi, Andrea Sabo, Twinkle Arora, Andrea Iaboni, and Babak Taati. The toronto older adults gait archive: video and 3d inertial motion capture data of older adults’ walking. *Scientific data*, 9(1):398, 2022. 1
- [45] Anat Mirelman, Hagar Bernad-Elazari, Avner Thaler, Eytan Giladi-Yacobi, Tanya Gurevich, Mali Gana-Weisz, Rachel Saunders-Pullman, Deborah Raymond, Nancy Doan, Susan B Bressman, et al. Arm swing as a potential new prodromal marker of parkinson’s disease. *Movement Disorders*, 31(10): 1527–1534, 2016. 5, 2
- [46] Meg E Morris, Robert Iansek, Thomas A Matyas, and Jeffery J Summers. The pathogenesis of gait hypokinesia in parkinson’s disease. *Brain*, 117(5):1169–1181, 1994. 1
- [47] Beatriz Muñoz-Ospina, Daniela Alvarez-Garcia, Hugo Juan Camilo Clavijo-Moran, Jaime Andrés Valderrama-Chaparro, Melisa García-Peña, Carlos Alfonso Herrán, Christian Camilo Urcuqui, Andrés Navarro-Cadavid, and Jorge Orozco. Machine learning classifiers to evaluate data from gait analysis with depth cameras in patients with parkinson’s disease. *Frontiers in Human Neuroscience*, 16:826376, 2022. 6
- [48] Kimberley-Dale Ng, Sina Mehdizadeh, Andrea Iaboni, Avril Mansfield, Alastair Flint, and Babak Taati. Measuring gait variables using computer vision to assess mobility and fall risk in older adults with dementia. *IEEE journal of translational engineering in health and medicine*, 8:1–9, 2020. 7
- [49] Koichiro Niinuma, Itir Onal Ertugrul, Jeffrey F Cohn, and László A Jeni. Synthetic expressions are better than real for learning to detect facial actions. In *Proceedings of the IEEE/CVF Winter Conference on Applications of Computer Vision*, pages 1248–1257, 2021. 2
- [50] Hyun-Jic Oh and Won-Ki Jeong. DiffMix: Diffusion model-based data synthesis for nuclei segmentation and classification in imbalanced pathology image datasets. In *International Conference on Medical Image Computing and Computer-Assisted Intervention*, pages 337–345. Springer, 2023. 2
- [51] Mathis Petrovich, Michael J Black, and Gül Varol. Action-conditioned 3d human motion synthesis with transformer vae. In *Proceedings of the IEEE/CVF International Conference on Computer Vision*, pages 10985–10995, 2021. 5
- [52] Mathis Petrovich, Michael J. Black, and Gül Varol. TEMOS: Generating diverse human motions from textual descriptions. In *European Conference on Computer Vision (ECCV)*, 2022. 5
- [53] Ekkasit Pinyoanuntapong, Pu Wang, Minwoo Lee, and Chen Chen. MMM: Generative masked motion model. In *Proceedings of the IEEE/CVF Conference on Computer Vision and Pattern Recognition*, pages 1546–1555, 2024. 2, 5, 6
- [54] Matthias Plappert, Christian Mandery, and Tamim Asfour. The kit motion-language dataset. *Big data*, 4(4):236–252, 2016. 2
- [55] Rahm Ranjan, David Ahmedt-Aristizabal, Mohammad Ali Armin, and Juno Kim. Computer vision for clinical gait analysis: A gait abnormality video dataset. *arXiv preprint arXiv:2407.04190*, 2024. 1, 2
- [56] Adrit Rao, Andrea Fisher, Ken Chang, John Christopher Panagides, Katherine McNamara, Joon-Young Lee, and Oliver Aalami. IMIL: Interactive medical image learning framework. In *Proceedings of the IEEE/CVF Conference on Computer Vision and Pattern Recognition*, pages 5241–5250, 2024. 7
- [57] Marcus Richards, Karen Marder, Lucien Cote, and Richard Mayeux. Interrater reliability of the unified parkinson’s disease rating scale motor examination. *Movement Disorders*, 9(1):89–91, 1994. 1, 7
- [58] Karl Ridgeway and Michael C Mozer. Learning deep disentangled embeddings with the f-statistic loss. *Advances in neural information processing systems*, 31, 2018. 2
- [59] Andrea Sabo, Sina Mehdizadeh, Andrea Iaboni, and Babak Taati. Estimating parkinsonism severity in natural gait videos of older adults with dementia. *IEEE journal of biomedical and health informatics*, 26(5):2288–2298, 2022. 5, 6, 7
- [60] Andrea Sabo, Andrea Iaboni, Babak Taati, Alfonso Fasano, and Carolina Gorodetsky. Evaluating the ability of a predictive vision-based machine learning model to measure changes in gait in response to medication and dbs within individuals with parkinson’s disease. *BioMedical Engineering OnLine*, 22(1):120, 2023. 1
- [61] Geise Santos, Marcelo Wanderley, Tiago Tavares, and Anderson Rocha. A multi-sensor human gait dataset captured through an optical system and inertial measurement units. *Scientific Data*, 9(1):545, 2022. 4
- [62] Mert Bülent Saryıldız, Karteek Alahari, Diane Larlus, and Yannis Kalantidis. Fake it till you make it: Learning transferable representations from synthetic imagenet clones. In *Proceedings of the IEEE/CVF Conference on Computer Vision and Pattern Recognition*, pages 8011–8021, 2023. 2
- [63] Céline Schreiber and Florent Moissenet. A multimodal dataset of human gait at different walking speeds established on injury-free adult participants. *Scientific data*, 6(1):111, 2019. 4
- [64] Thiago Kenzo Fujioka Shida, Thaisy Moraes Costa, Claudia Eunice Neves de Oliveira, Renata de Castro Treza, Sandy Mikie Hondo, Emanuele Los Angeles, Claudionor Bernardo, Luana dos Santos de Oliveira, Margarete de Jesus Carvalho, and Daniel Boari Coelho. A public data set of walking full-body kinematics and kinetics in individuals with parkinson’s disease. *Frontiers in Neuroscience*, 17:992585, 2023. 5, 7, 6
- [65] Soyong Shin, Juyong Kim, Eni Halilaj, and Michael J. Black. WHAM: Reconstructing world-grounded humans with accurate 3D motion. In *IEEE/CVF Conf. on Computer Vision and Pattern Recognition (CVPR)*, 2024. 5, 6
- [66] Wenfeng Song, Xingliang Jin, Shuai Li, Chenglizhao Chen, Aimin Hao, Xia Hou, Ning Li, and Hong Qin. Arbitrary motion style transfer with multi-condition motion latent diffusion model. In *Proceedings of the IEEE/CVF Conference on Computer Vision and Pattern Recognition*, pages 821–830, 2024. 2, 5

- [67] Ömer Sümer, Tobias Huber, Dat Duong, Suzanna E Ledgister Hanchard, Cristina Conati, Elisabeth André, Benjamin D Solomon, and Rebekah L Waikel. Evaluation of a deep learning and xai based facial phenotyping tool for genetic syndromes: A clinical user study. *medRxiv*, pages 2025–06, 2025. 7
- [68] Tianxin Tao, Xiaohang Zhan, Zhongquan Chen, and Michiel van de Panne. Style-ERD: Responsive and coherent online motion style transfer. In *Proceedings of the IEEE/CVF Conference on Computer Vision and Pattern Recognition*, pages 6593–6603, 2022. 2
- [69] Guy Tevet, Sigal Raab, Brian Gordon, Yoni Shafir, Daniel Cohen-or, and Amit Haim Bermano. Human motion diffusion model. In *The Eleventh International Conference on Learning Representations*, 2023. 2, 6
- [70] Sjoerd Van Steenkiste, Francesco Locatello, Jürgen Schmidhuber, and Olivier Bachem. Are disentangled representations helpful for abstract visual reasoning? *Advances in neural information processing systems*, 32, 2019. 2
- [71] Diwei Wang, Čađđric Bobenrieth, and Hyewon Seo. Agir: Assessing 3d gait impairment with reasoning based on llms. *arXiv preprint arXiv:2503.18141*, 2025. 7
- [72] Tan Wang, Linjie Li, Kevin Lin, Yuanhao Zhai, Chung-Ching Lin, Zhengyuan Yang, Hanwang Zhang, Zicheng Liu, and Lijuan Wang. DisCo: Disentangled control for realistic human dance generation. In *Proceedings of the IEEE/CVF Conference on Computer Vision and Pattern Recognition*, pages 9326–9336, 2024. 2
- [73] Yaohui Wang, Piotr Bilinski, Francois Bremond, and Antitza Dantcheva. G3AN: Disentangling appearance and motion for video generation. In *Proceedings of the IEEE/CVF Conference on Computer Vision and Pattern Recognition*, pages 5264–5273, 2020. 2
- [74] Zhizhong Wang, Lei Zhao, and Wei Xing. StyleDiffusion: Controllable disentangled style transfer via diffusion models. In *Proceedings of the IEEE/CVF International Conference on Computer Vision*, pages 7677–7689, 2023. 2
- [75] Zhicai Wang, Longhui Wei, Tan Wang, Heyu Chen, Yanbin Hao, Xiang Wang, Xiangnan He, and Qi Tian. Enhance image classification via inter-class image mixup with diffusion model. In *Proceedings of the IEEE/CVF Conference on Computer Vision and Pattern Recognition*, pages 17223–17233, 2024. 2
- [76] Will Williams, Sam Ringer, Tom Ash, David MacLeod, Jamie Dougherty, and John Hughes. Hierarchical quantized autoencoders. *Advances in Neural Information Processing Systems*, 33:4524–4535, 2020. 6
- [77] Qiucheng Wu, Yujian Liu, Handong Zhao, Ajinkya Kale, Trung Bui, Tong Yu, Zhe Lin, Yang Zhang, and Shiyu Chang. Uncovering the disentanglement capability in text-to-image diffusion models. In *Proceedings of the IEEE/CVF conference on computer vision and pattern recognition*, pages 1900–1910, 2023. 2
- [78] Yiming Xie, Varun Jampani, Lei Zhong, Deqing Sun, and Huaizu Jiang. OmniControl: Control any joint at any time for human motion generation. *arXiv preprint arXiv:2310.08580*, 2023. 2
- [79] Zikang Xu, Jun Li, Qingsong Yao, Han Li, Mingyue Zhao, and S Kevin Zhou. Addressing fairness issues in deep learning-based medical image analysis: a systematic review. *npj Digital Medicine*, 7(1):286, 2024. 1
- [80] Wenjie Yin, Hang Yin, Kim Baraka, Danica Kragic, and Mårten Björkman. Dance style transfer with cross-modal transformer. In *Proceedings of the IEEE/CVF Winter Conference on Applications of Computer Vision*, pages 5058–5067, 2023. 2
- [81] Jianrong Zhang, Yangsong Zhang, Xiaodong Cun, Yong Zhang, Hongwei Zhao, Hongtao Lu, Xi Shen, and Ying Shan. Generating human motion from textual descriptions with discrete representations. In *Proceedings of the IEEE/CVF conference on computer vision and pattern recognition*, pages 14730–14740, 2023. 2, 4
- [82] Mingyuan Zhang, Huirong Li, Zhongang Cai, Jiawei Ren, Lei Yang, and Ziwei Liu. FineMoGen: Fine-grained spatio-temporal motion generation and editing. *Advances in Neural Information Processing Systems*, 36:13981–13992, 2023. 2
- [83] Qitao Zhao, Ce Zheng, Mengyuan Liu, Pichao Wang, and Chen Chen. Poseformerv2: Exploring frequency domain for efficient and robust 3d human pose estimation. In *Proceedings of the IEEE/CVF conference on computer vision and pattern recognition*, pages 8877–8886, 2023. 6
- [84] Yi Zhou, Connelly Barnes, Jingwan Lu, Jimei Yang, and Hao Li. On the continuity of rotation representations in neural networks. In *Proceedings of the IEEE/CVF conference on computer vision and pattern recognition*, pages 5745–5753, 2019. 4
- [85] Zixiang Zhou, Yu Wan, and Baoyuan Wang. AvatarGPT: All-in-one framework for motion understanding planning generation and beyond. In *Proceedings of the IEEE/CVF Conference on Computer Vision and Pattern Recognition*, pages 1357–1366, 2024. 4
- [86] Xinxin Zuo, Sen Wang, Jiangbin Zheng, Weiwei Yu, Minglun Gong, Ruigang Yang, and Li Cheng. SparseFusion: Dynamic human avatar modeling from sparse rgbd images. *IEEE Transactions on Multimedia*, 23:1617–1629, 2020. 6

Appendix

Supplemental Video. Our model generates gait sequences that depict the movement impairments associated with PD. The supplemental video provides qualitative demonstrations that illustrate these motion dynamics and subtle PD-related features in a way that still images cannot. We strongly recommend that readers view the provided supplemental video.

Further clarification on “Motion” and “Pathology” terms.

In our work, “Motion” denotes the *general* gait biomechanics (e.g., alternating heel strikes) or the inherent physiological motion constraints (e.g., limited range of motion in knee flexion and extension). “Pathology”, on the other hand, describes disease-specific patterns **absent** in healthy gait (e.g., small, shuffling steps, reduced arm swing, festination, etc.). Our model explicitly separates these factors by learning a distinct pathology latent space, ensuring that pathology-related deviations are captured independently of normal motion dynamics. This disentanglement allows for precise control over gait synthesis, enabling pathology-conditioned generation while preserving natural locomotion patterns.

A. More on Clinical Validity

A.1. Elaboration on Clinical Motivation

Parkinsonian gait analysis has direct clinical relevance, particularly in early detection and continuous monitoring. Yet, the scarcity of annotated data for severe PD stages, where motor symptoms become most pronounced, restricts the ability of machine learning models to generalize [2]. Our synthetic generation approach mitigates this data imbalance by creating realistic, pathology-specific gait samples. This enriched training set ultimately supports more robust detection and staging tools, which could improve clinical workflows and inform therapeutic decisions without requiring extensive additional data collection. This approach could also reduce the burden of collecting large amounts of new clinical data.

A.2. Quantitative Validation of SMPL Estimation for Clinical Gait Analysis

To establish the clinical reliability of SMPL-based representations used in PD-GaM, we validated the outputs of WHAM, the mesh extraction backbone used for our dataset, against an external biomechanical benchmark with ground-truth kinematics. The Toronto Older Adults Gait Archive (TOAGA) [44] was selected for this purpose because it uniquely satisfies three key criteria: (i) provides synchronized RGB video and gold-standard full-body 3D motion data from Xsens MVN Analyze IMUs (from 14 participants), (ii) involves straight-walking trials comparable to PD-GaM, and (iii) features an older-adult cohort relevant to parkinsonian

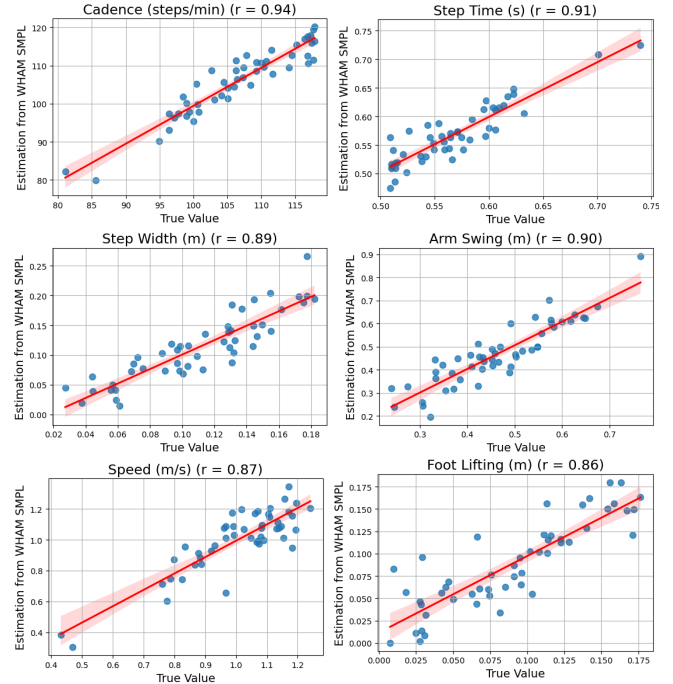


Figure S7. WHAM-derived SMPL estimates vs. Xsens ground truth for six gait features in TOAGA; strong correlations ($r = 0.86 - 0.94$) confirm biomechanical fidelity.

studies.

From each TOAGA walk we extracted cadence, walking speed, step time, step width, arm swing amplitude, and foot lifting height from WHAM meshes (features that are clinically meaningful for parkinsonian gait and present in the dataset) and compared them with the same features computed from IMU. Pearson correlations ranged from $r = 0.86$ to $r = 0.94$ (Fig. S7), indicating strong agreement closely matching the high video-vs-IMU correlations reported in the original TOAGA paper; confirming that WHAM preserves clinically relevant gait dynamics.

To assess geometric accuracy, we computed the root-relative MPJPE between WHAM-extracted joints and synchronized Xsens ground truth, obtaining an average error of 39 mm. This falls within the 35–65 mm band reported for multi-view pose estimation systems [3, 6, 31] and the TULIP dataset for PD gait task [33].

Together, the strong spatiotemporal correlations and low geometric error demonstrate that WHAM-derived SMPL meshes are a reliable surrogate for markerless gait analysis in our study. Nevertheless, while WHAM is used in this study, our method is not tied to it and is expected to benefit from

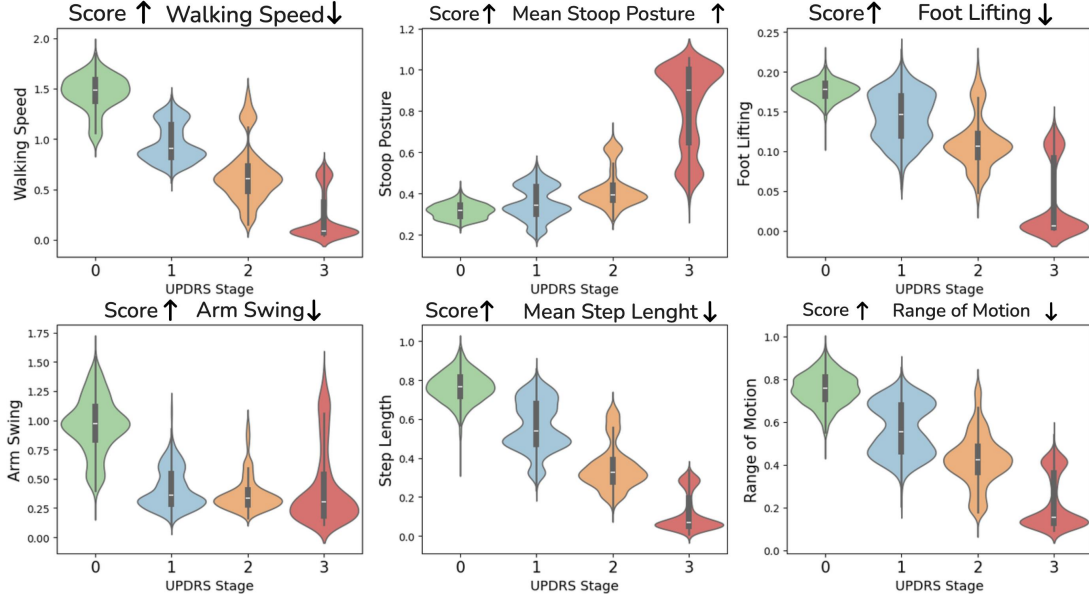


Figure S8. Distributions of gait features from $8k$ synthesized GAITGen sequences across UPDRS stages. Walking speed, step length, foot lifting, arm swing, and ROM decline with severity, with the steepest drop at UPDRS 3. Stoop posture increases sharply at stage 3.

| | | | |
|---------------------|------|----------------|---------------------|
| | Real | 0.54 | 0.46 |
| Synthetic (GAITGen) | | 0.51 | 0.49 |
| | | Judged as real | Judged as synthetic |

Figure S9. User study ($n=6$) on distinguishing real vs. synthetic data generated by GAITGen.

improvements in mesh estimation quality.

A.3. Clinical Gait Features Validation

We extracted six clinically relevant features from $8k$ GAITGen synthetic sequences and plotted their distributions by UPDRS stage (Fig. S8). Walking speed and mean step length consistently decrease with higher UPDRS scores, with a pronounced drop at stage 3, indicating severe motor impairment. Mean stoop posture increases sharply at stage 3, reflecting the stooped posture typical of advanced Parkinsonian gait. Foot lifting and arm swing both decline across stages, again with the steepest reduction at UPDRS 3. Range of motion (ROM) shows a gradual decrease with increasing severity, suggesting reduced joint mobility. The alignment of these trends with established clinical observations [30, 45] supports the validity of GAITGen’s severity-conditioned synthesis. See Sec. J for more details on the gait features calculation.

A.4. Additional Clinical User Study Results

Our 6 clinical raters completed a tutorial with paired videos/SMPL avatars before blind evaluation. Since clinical evaluation focuses on parkinsonian gait features (not facial or

clothing cues) scoring avatar meshes is equivalent to video. For fairness, all real sequences were also rendered to SMPL meshes. The evaluation was fully blind which means raters saw only meshes, without knowing whether a sequence was real or synthetic or how many of each were included. Clinicians easily recognised parkinsonian features from rendered mesh, supported by strong agreement with GT video scores (0.91) and near-chance real vs. synthetic discrimination (precision=0.52, S9), confirming clinical validity of the mesh avatar format. Fig. S9 shows the confusion matrix for the real vs. synthetic classification task in the clinical user study described in the main manuscript. The near chance-level performance by clinicians highlights the high visual realism of GAITGen’s outputs.

A.5. Interpretation of Interference Weight α

The interference weight α modulates the contribution of pathology-specific features in the reconstructed gait sequences. Experiments with $\alpha = 0.2, 0.5, 1.0$ revealed a trade-off: Lower values of α prioritize motion dynamics over pathology features, slightly improving reconstruction, but reducing classification accuracy of ϕ_p for severe pathology (UPDRS-gait score 3). Fig. S10 presents the confusion matrices of the classifier ϕ_p for different α values. Our final model uses $\alpha = 1.0$ to achieve better performance on severe cases, while α remains adjustable depending on specific application requirements.

To examine whether pathology is controllably expressed in the latent space, we conducted a mix-and-match experiment in which motion latent (\mathbf{q}_m) from a UPDRS 0 sequence were combined with pathology latent (\mathbf{q}_p) from a UPDRS 3 sequence and scaled by α . As shown in Fig. S11, the predicted

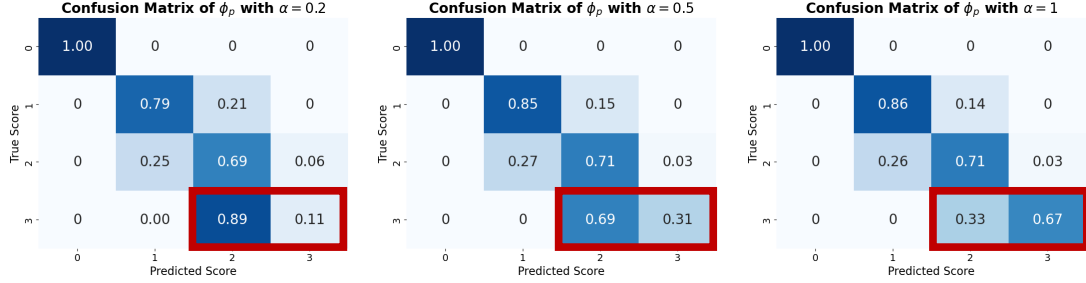


Figure S10. Confusion matrices of the classifier ϕ_p for different values of interference weight α .

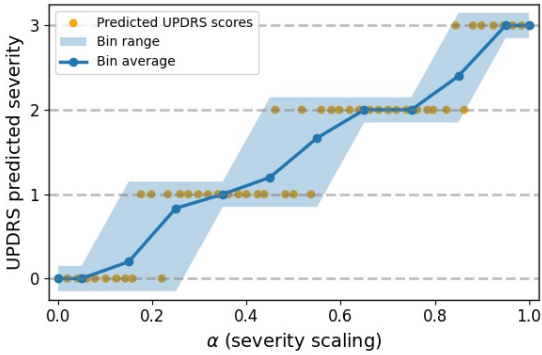


Figure S11. Predicted UPDRS-gait severity as a function of interference weight α . Motion latent (\mathbf{q}_m) from a UPDRS 0 sequence were combined with pathology latent (\mathbf{q}_p) from a UPDRS 3 sequence. Orange points show discrete classifier predictions for synthetic samples generated by varying α from 0 to 1. Blue shading denotes the min-max prediction range within 0.1-wide bins, and the blue curve indicates the bin-wise mean.

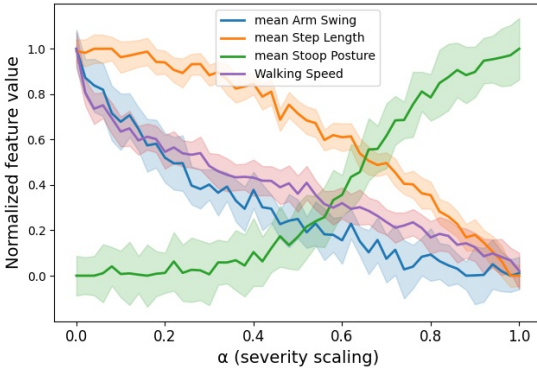


Figure S12. Interpretation of α through four gait features. Lines show mean values and shaded regions denote standard deviations across generated samples.

UPDRS-gait severity increases monotonically as α is varied from 0 to 1. At low values of α , predictions remain in the healthy range, while higher values shift decoded motions and predictions toward severe impairment.

To better interpret α , we combined motion latents from ten samples with UPDRS score = 0 sequences with pathology latents from five UPDRS 3 sequences, generating 50 synthetic samples per ranging value of α . Fig. S12 summarizes the

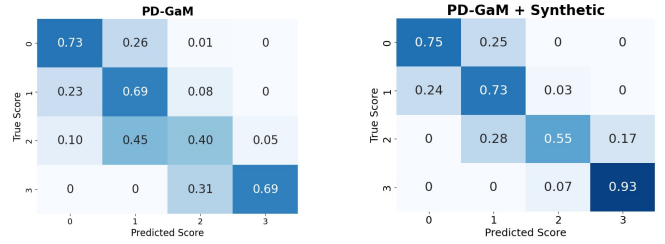


Figure S13. Confusion matrix of downstream classifiers trained on (left) PD-GaM (right) PD-GaM+Synthetic data.

resulting gait features. On average, arm swing, step length, and walking speed decrease with increasing α , while stoop posture increases. These feature-level trends align with established Parkinsonian gait characteristics. These results also provide strong evidence that the model achieved disentanglement of motion and pathology, enabling clinically coherent severity modulation.

A.6. Downstream Classifier details and Confusion Matrices

For the downstream classification task we used three different pre-trained models and a Random Forest on clinical gait features (Tab. 3 in the paper). Motion embeddings extracted from these encoders are fed into a lightweight trainable classifier head with three fully connected layers (hidden sizes: (128, 64)) to predict UPDRS-gait severity levels. The classifier is trained on the PD-GaM training set along with synthetic data and evaluated *only* on real samples from the PD-GaM test split. The confusion matrices in Fig. S13 compare our primary classifier's (ConvAutoEnc) performance when trained on (left) the PD-GaM training set alone (right) PD-GaM combined with synthetic data, both tested on the same real PD-GaM test set. Adding synthetic data improves UPDRS classification, especially for severe cases (score 3).

B. More on Mix and Match Augmentation.

Mix and Match augmentation is not a naive data augmentation technique. It leverages the decoder's capacity to integrate motion and pathology features. The decoder determines the final output by considering the input motion, the pathol-

ogy severity level, and their likelihoods, resulting in coherent and realistic gait sequences. For instance, in qualitative results shown in Fig.8 (manuscript), when a severe pathology (score 3) is paired with a motion where the person walks a long distance, the decoder adapts the trajectory to reflect the constraints of severe pathology, which typically limits walking distance. This demonstrates that our method goes beyond naive augmentation by producing contextually appropriate modifications based on the severity level. However, while Mix and Match is effective for augmenting underrepresented classes, it is limited in diversity and control. It serves as a supplementary technique suitable for small-scale augmentation but does not replace the need for training our generative model.

For clarity, GAITGen is purpose-built for *pathology-conditioned* gait generation, isolating pathology indicators from general motion patterns to synthesize gaits that reflect a specific severity level. Modeling subject identity is out of scope, as it shifts focus from pathology modeling to personalization, unnecessary for our data augmentation purpose and could compromise generalization and privacy.

B.1. Alternate Latent Fusion Strategy.

An alternative motion and pathology latent fusion is elementwise multiplication of \mathbf{q}_m and \mathbf{q}_p . We choose addition, $\mathcal{D}(\mathbf{q}_m + \alpha \cdot \mathbf{q}_p)$, over elementwise multiplication, $\mathcal{D}(\mathbf{q}_m \odot \mathbf{q}_p)$, for *optimization stability*. Addition behaves as residual learning, where the pathology vector only needs to encode scale-independent corrections. With addition, the zero vector naturally preserves the healthy baseline motion, and small errors from the pathology branch do not distort the underlying motion. In contrast, with multiplication, the network must learn to output \mathbf{q}_m close to one in this case, and even small deviations can disproportionately affect the representation (e.g., if \mathcal{E}_p outputs 0.9 instead of 1, the healthy subcode is reduced by 10% across all dimensions, regardless of whether this change is meaningful). Moreover, gradients under multiplication scale with the magnitude of latents, making optimization unstable and scale-sensitive, whereas in the addition, gradients remain scale independent. This makes addition both more robust and consistent with residual formulations widely used in deep learning architectures.

C. Training with Additional Gait Data.

To test whether healthy gait datasets can compensate for the limited pathological data, we added four external healthy gait datasets [5, 21, 61, 63] (7,971 walks) to the training set. As shown in Tab. S7, this led to only minor gains. Given the relative simplicity of the walking motion, healthy gait is already well-modeled. The main challenge is modeling pathological deviations. Thus, additional normal samples offer limited value and can even bias the model toward UPDRS 0, weakening the pathology latent. To prevent this, we use the extra

| | MPJPE ↓ | PAMPJPE ↓ | ACCL ↓ | DS ↑ | AVE ↓ |
|---------------------------|---------|-----------|--------|------|-------|
| GAITGen | 28.38 | 17.91 | 15.35 | 1.21 | 0.19 |
| + Additional Healthy Gait | 28.01 | 17.43 | 15.29 | 1.24 | 0.18 |

Table S7. Impact of additional healthy gait.

healthy data only to pretrain the motion encoder \mathcal{E}_m , keeping the pathology encoder \mathcal{E}_p trained exclusively on PD gait. These results confirm that future gains will come from more diverse pathological data, not from additional healthy walks.

D. Implementation Details

Model encoders are 1D convolutional ResNet blocks with a temporal downsampling rate of 4. The decoder \mathcal{D} mirrors the encoders’ architecture. \mathcal{E}_m is pretrained for 200 epochs (learning rate (lr) $2e^{-6}$) with a reduced lr factor of 0.1 during joint training with \mathcal{E}_p (lr $2e^{-6}$) and the classifiers (lr $2e^{-7}$) for 300 epochs. The loss weights are set as $\lambda_r = 1$, $\lambda_c = \lambda_{adv} = 0.01$, and $\lambda_{emb} = 0.02$. We adopt a quantization dropout strategy, with a probability of 0.2. N is set to 6, and both motion and pathology codebook dimensions are 64, with codebook sizes of 512 for motion and 128 for pathology with $\alpha = 1$ for the final model. For the \mathcal{M}_θ and the \mathcal{R}_θ , we use a lr of $1e^{-3}$ with Adam schedule-free optimizers [14]. The mini-batch size is set to 512 for RVQ-VAE and 256 for the transformers.

VQ-VAE. We employ a 1D convolutional ResNet-based encoder-decoder for gait sequence modeling. The encoder downsamples the input sequence through two convolutional ResNet blocks, reducing the temporal resolution by $4\times$. Initially, a conv layer maps the D -dimensional input motion to $D_m = D_p = 64$ channels, followed by temporal downsampling and quantization into $\#cb_m = 512$ motion and $\#cb_p = 128$ pathology codebooks, each with 64-dimensional embeddings. The decoder mirrors the encoder to reconstruct the motion sequence using upsampling ResNet blocks, thereby restoring the original temporal resolution. It also includes one conv layer to recover the original channel size.

Transformers. To ensure diversity in generated sequences, GAITGen integrates residual stochastic sampling techniques, inspired by language modeling approaches such as BERT [32]. During inference, mask tokens are *re-drawn at every sampling step* following a cosine-decay schedule. We apply Top-K filtering and remasking plus Gumbel sampling to enhance diversity. Specifically, in an iterative 10-step process, the top 10% of predicted tokens are retained (based on predicted probabilities), while the remaining 90% are re-masked for refinement. So, the only element that remains constant is the pathology *condition*; neither motion nor pathology tokens are tied to a fixed mask. Therefore, two identical motion seeds are masked differently and converge to distinct completions, ensuring diversity. During training, we introduce additional stochasticity by replacing selected

masked tokens with random tokens 8% of the time instead of `<mask>` to enhance robustness. We used CLIP encoding followed by a projection layer for condition, with the four-class c_p functioning similarly to action or style conditioned motion generation [51, 66].

E. Additional Experiments.

Number of Quantization Layer. Tab. S8 shows that increasing the number of quantization layers from 1 to 6 leads to consistent improvements in reconstruction metrics and generation quality (lower AVE). This is because additional layers allow the model to capture finer-grained details of the gait sequences. However, beyond 6 layers, we observe marginal gains in reconstruction and a slight decline in generation performance. This may be due to the increased complexity, making it more challenging for the residual transformer \mathcal{R}_θ to predict higher-order residuals effectively. Additionally, more layers introduce higher computational costs with diminished disentanglement (lower DS) without significant benefits. Therefore, we selected 6 quantization layers for GAIT-Gen as it offers a good trade-off between reconstruction fidelity and generation quality.

| #Quantization layer(s) | Reconstruction | | | | Generation |
|------------------------|----------------|--------------|--------------|-------------|-------------|
| | MPJPE ↓ | PAMPJPE ↓ | ACCL ↓ | DS ↑ | AVE ↓ |
| 1 | 58.42 | 26.11 | 25.07 | 0.77 | 0.62 |
| 2 | 51.78 | 24.56 | 22.43 | 0.92 | 0.46 |
| 3 | 43.90 | 21.87 | 19.76 | 1.15 | 0.47 |
| 4 | 35.77 | 19.98 | 17.43 | 1.02 | 0.32 |
| 5 | 31.83 | 18.51 | 15.67 | 1.24 | 0.24 |
| 6 | 28.38 | 17.91 | 15.35 | 1.21 | 0.19 |
| 7 | 27.92 | 17.12 | 15.11 | 0.95 | 0.21 |
| 8 | 27.15 | 16.94 | 15.14 | 0.88 | 0.25 |

Table S8. Impact of the number of quantization layers on model performance.

Motion Encoder Reduced Learning Rate Factor. We examine how reducing the learning rate (lr) of the motion encoder \mathcal{E}_m during fine-tuning with the pathology encoder influences disentanglement. As shown in Tab. S9, using an lr reduction factor of 0.1 increases the DS from 0.94 to 1.21. With an lr factor of 1 (no reduction), the motion encoder updates quickly under the influence of the adversarial classifier, causing it to unlearn essential motion features, which degrades reconstruction quality. To compensate, the pathology encoder begins capturing motion information, compromising disentanglement and reducing the DS. Conversely, very small lr factors (0.01 and 0.001) lead to insufficient adjustments by the motion encoder, leaving residual pathology information in the motion latent space and resulting in a lower DS.

Number of Inference Iterations and Masking Scheduler. Here we investigate how the number of inference iterations and the choice of scheduler influence the performance of the Mask Transformer \mathcal{M}_θ . During iterative refinement, the

| \mathcal{E}_m lr factor | MPJPE ↓ | PAMPJPE ↓ | ACCL ↓ | DS ↑ |
|---------------------------|--------------|--------------|--------------|-------------|
| 1 | 28.19 | <u>17.84</u> | <u>15.31</u> | 0.94 |
| 0.1 | <u>28.38</u> | <u>17.91</u> | <u>15.35</u> | 1.21 |
| 0.01 | 28.71 | 18.23 | 17.01 | 1.11 |
| 0.001 | 29.94 | 19.29 | 17.06 | 0.86 |

Table S9. Impact of learning rate reduction factors for the motion encoder \mathcal{E}_m during fine-tuning. Best results are in **bold**, comparable results are underlined.

masking ratio $\beta(t)$ determines the proportion of tokens to re-mask at each iteration, with t representing the normalized timestep from 0 to 1 over R iterations (i.e., $t = \frac{\text{current iteration}}{R}$). Two schedulers are compared: the linear scheduler ($\beta(t) = 1 - t$) decreases the masking ratio uniformly, while the cosine scheduler ($\beta(t) = \cos(\frac{\pi t}{2})$) maintains a higher masking ratio initially, gradually reducing it in later iterations. This higher masking ratio allows the cosine scheduler to focus on easier-to-predict tokens first and progressively tackle harder tokens in later iterations. During training, t is sampled uniformly ($t \sim \mathcal{U}(0, 1)$), and during inference, t is deterministically stepped from 0 to 1 over R iterations. At each iteration, the number of tokens to be masked is calculated as $\beta(t) \times M$, where $M = 2T' + 1$ is the total number of tokens in the sequence. Tab. S10 shows that the cosine scheduler consistently outperforms the linear one, especially at fewer iterations, indicating faster convergence.

| #Iterations (Scheduler) | AVE ↓ | AAMD ↓ | ASMD ↓ | Div → |
|-------------------------|--------------|--------------|--------------|--------------|
| 5 (linear) | 0.367 | 0.165 | 0.071 | 3.744 |
| 10 (linear) | 0.294 | 0.142 | 0.049 | 3.906 |
| 20 (linear) | 0.217 | 0.103 | 0.051 | 3.911 |
| 5 (cosine) | 0.313 | 0.134 | 0.066 | 3.824 |
| 10 (cosine) | 0.194 | 0.096 | 0.048 | 3.966 |
| 20 (cosine) | 0.194 | 0.099 | 0.047 | 3.957 |

Table S10. Impact of inference iterations and scheduler type of the mask transformer model.

VAE Channel Size. The channel size in the VAE determines the number of feature channels in intermediate layers, influencing model’s representational capacity. Experiments with varying channel sizes (Tab. S11) show a channel size of 512 achieves the best overall performance, outperforming smaller channel sizes. Increasing the size to 1024 marginally improves ACCL but comes at the cost of increased computational complexity without meaningful benefits to other metrics.

| \mathcal{E}_m #Channel | MPJPE ↓ | PAMPJPE ↓ | ACCL ↓ | DS ↑ |
|--------------------------|--------------|--------------|--------------|-------------|
| 128 | 58.31 | 27.65 | 25.98 | 0.76 |
| 256 | 39.08 | 21.78 | 19.97 | 0.94 |
| 512 | 28.38 | 17.91 | 15.35 | 1.21 |
| 1024 | 29.12 | 17.95 | 15.23 | 1.14 |

Table S11. Impact of VAE channel size on model performance.

Findings on Codebook Learning. We conducted an experiment to examine the effects of increasing the codebook commitment loss weight (λ_{emb}) and incorporating periodic codebook reset strategy [76] in the quantization process. Raising λ_{emb} from 0.02 to 0.09 resulted in stronger commitment of input vectors to specific codebook entries. However, this came at the cost of worse reconstruction quality and severity prediction performance from pathology latents \mathbf{q}_p . A higher λ_{emb} caused the model to commit to a subset of codebook entries early, leaving others unused. We also experimented with periodic codebook resets, where unused codebook entries are reset to random values every 20 iterations instead of at every iteration, giving the codebooks more opportunity to be used before being reset. However, we found that the introduction of new, randomly initialized entries after multiple iterations disrupted the model’s established encoding patterns, leading to instability and degraded performance. In contrast, when using a lower λ_{emb} (0.02) with codebook resets at every iteration, the model’s commitment to codebook entries was less rigid, allowing the model to adapt more smoothly to the resets without significant disruption, resulting in the most optimal performance.

F. Latent space visualization

We present UMAP visualizations of the latent space in Fig. S14. GAITGen achieves well-clustered latent representations aligned with UPDRS-gait scores. Without condition (\mathcal{E}_p) or disentanglement, the clusters displays significant overlap among classes.

G. Datasets

G.1. PD-GaM.

PD-GaM is a large PD Gait 3D Mesh dataset derived from the PD4T dataset; but it is anonymized for public release. The original PD4T dataset included 426 gait video recordings from 30 individuals with PD. Each participant in PD4T was asked to walk forward and backward twice, resulting in 4 walking segments per participant and 1701 walk (≈ 3 hours) in total. Each recording was reviewed and segmented to retain usable gait segments while excluding frames involving turns. Turns present a unique challenge for individuals with PD, as the gait changes observed during turns differ significantly from those seen during walking. To maintain a consistent representation of gait patterns, only walking sequences are included in this paper. However, we plan to also release the turn segments in PD-GaM to support research on turn-specific gait analysis. SMPL parameters for each subject were extracted at 25 FPS using the WHAM [65]. The camera, positioned at eye level and following the subjects as they walked in original videos, introduced minor distortions in global trajectories. These distortions were corrected during preprocessing to minimize global position artifacts. The

dataset is divided into training (1253 samples) and test (448 samples) sets using a participant-based split to ensure unbiased evaluation. A histogram of UPDRS-gait scores in PD-GaM is presented in Fig. S15, highlighting the imbalance in class representation, particularly the limited number of samples in the severe category (class 3). This scarcity emphasizes the importance of our Mix and Match augmentation strategy.

G.2. External Datasets.

The T-SDU-PD dataset [59] contains parkinsonian gait samples from 14 participants, each annotated per walk with UPDRS-gait scores by expert clinicians. Recordings were captured using a ceiling-mounted camera, and 3D meshes were extracted with WHAM [65]. The dataset includes 381 walking trials, totaling approximately 50 minutes.

The BMClab dataset [64] was collected with a Raptor-4 optical motion-capture system (Motion Analysis Corp.) using 44 reflective markers. It contains 781 walking trials (48 minutes) from PD participants, with MDS-UPDRS gait labels assigned at the participant level by expert clinicians. 3D meshes were obtained using SparseFusion optimization [86] to fit SMPL parameters from sparse 3D joints.

H. Input Motion Representation

Our motion representation follows the HumanML3D format [22]. Each frame is encoded as a 263-dimensional vector derived from the SMPL mesh representation of WHAM [65], with joints mapped to 22 AMASS joints [43]. This representation includes root angular velocity ($r^a \in \mathbb{R}$) along the Y-axis, root linear velocities ($r^x, r^z \in \mathbb{R}$) on the XZ-plane, root height ($r^y \in \mathbb{R}$), local joint positions ($j^p \in \mathbb{R}^{3N_j}$), joint velocities ($j^v \in \mathbb{R}^{3N_j}$), joint rotations ($j^r \in \mathbb{R}^{6N_j}$), and binary foot-ground contact features ($c^f \in \mathbb{R}^4$). This redundant representation captures both kinematic and dynamic properties, making it suitable for neural models, particularly generative frameworks. It also allows for the disentanglement of motion dynamics from pathology-specific characteristics.

I. Metric Details

Here we provide details of the AVE, AAMD, and ASMD metrics. All reported generation results are averaged over 10 repetitions.

Average Variance Error (AVE) measures how closely the variance of local joint positions in the generated poses matches the ground-truth variance. For each joint j , the variance $\sigma[j]$ is computed as:

$$\sigma[j] = \frac{1}{T-1} \sum_{t \in T} (P_t[j] - \bar{P}[j])^2 \quad (5)$$

where $\bar{P}[j]$ is the mean position for joint j across T frames.

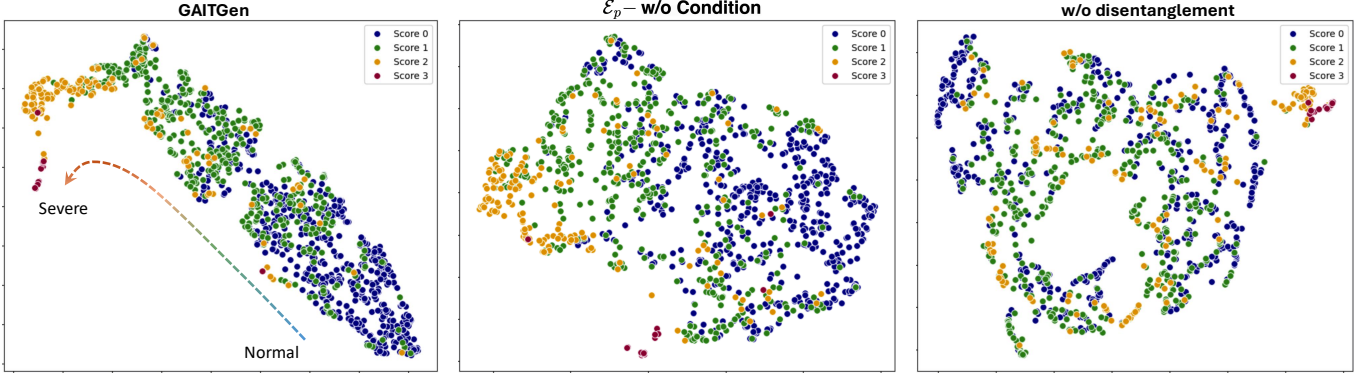


Figure S14. UMAP visualizations of the latent space representations under different settings. The left panel shows GAITGen with well-clustered latent representations aligned with UPDRS-gait scores. The middle panel represents the latent space when \mathcal{E}_p is unconditional, exhibiting overlap among classes. The right panel shows the results without disentanglement, further highlighting increased overlap and less separation of latent clusters.

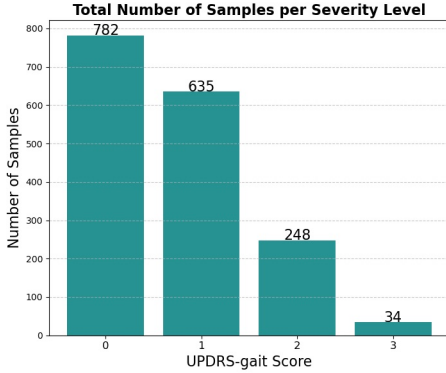


Figure S15. Histogram of UPDRS-gait scores in our PD-GaM dataset.

The AVE for each joint is then defined as:

$$\text{AVE}[j] = \frac{1}{N} \sum_{n \in N} \|\sigma[j] - \hat{\sigma}[j]\|_2 \quad (6)$$

where $\sigma[j]$ and $\hat{\sigma}[j]$ are the variances of joint j in the ground-truth and generated poses, respectively. The overall AVE is obtained by averaging the per-joint AVE values.

Absolute Arm Swing Mean Difference (AAMD) measures how closely the generated gait sequences replicate the arm swing ranges of the ground-truth data across different severity classes. For each class c , we calculate the mean arm swing range for the ground-truth ($\overline{AS}_{gt}^{(c)}$) and the generated ($\overline{AS}_{gen}^{(c)}$) sequences. The arm swing range for each sequence is computed by measuring the Euclidean distances between the wrist and shoulder joints at each time step, finding the maximum and minimum distances over the sequence, normalizing by leg length, and selecting the minimum arm swing between the two arms. The AAMD is then defined as the average of the absolute differences between these class-wise mean arm

swing ranges:

$$\text{AAMD} = \frac{1}{C} \sum_{c=1}^C \left| \overline{AS}_{gen}^{(c)} - \overline{AS}_{gt}^{(c)} \right| \quad (7)$$

where C is the total number of classes. A lower AAMD indicates that the generated sequences closely match the real arm swing patterns.

Absolute Stooped Posture Mean Difference (ASMD) quantifies how well the generated gait sequences replicate the stooped posture characteristic across different classes. Similar to AAMD, for each class, we compute the mean stooped posture for the ground-truth ($\overline{SP}_{gt}^{(c)}$) and generated ($\overline{SP}_{gen}^{(c)}$) sequences by calculating the vertical distance between the neck and sacrum joints at each time step for each sequence, averaging these distances over all frames, and normalizing by leg length. The ASMD is defined as the average of the absolute differences between these class-wise mean stooped postures:

$$\text{ASMD} = \frac{1}{C} \sum_{c=1}^C \left| \overline{SP}_{gen}^{(c)} - \overline{SP}_{gt}^{(c)} \right| \quad (8)$$

J. Gait Feature Extraction Details

We derive six clinically relevant features (i.e., Walking Speed, Mean Step Length, Arm Swing, Foot Lifting, Mean Stoop Posture, and Lower-Limb Range of Motion (ROM)) from generated SMPL joints to create an interpretable baseline for UPDRS-gait classification. Following [48], we first detected heelstrike frames by locating alternating peaks in the ankle-to-ankle distance (≤ 8 frames apart, prominence ≤ 0.02). Using these events and the normalized pose by leg length, we compute:

- Walking Speed: total sacrum displacement between first and last heel strike, divided by total time.

- Mean Step Length: Average ankle distance along walking axis between heel strikes.
- Arm Swing: horizontal displacement of the hand joints along the forward axis (sacrum-centered).
- Foot Lifting: vertical range of ankle movement.
- Stoop Posture: measured as the forward-lean distance which is the vertical displacement between neck and sacrum, projected onto the direction of walk.
- Range of Motion: maximum joint displacement, defined as the largest difference between a joint's maximum and minimum positions over time across all joints and axes.

All features are extracted from sequences aligned to a canonical (z-forward) frame.

K. Limitations

The current dataset scoring is based on gait segments that also include turning task, which may influence the UPDRS-gait scores. To address this, we are preparing revised scores focused exclusively on walking segments and will release both formats to accommodate different research objectives. Additionally, the dataset exhibits class imbalance, particularly in severe pathology cases with limited samples. Although our augmentation strategy helped mitigate this issue, integrating additional PD datasets standardized to the PD-GaM format could enhance generalizability and diversity of the generated sequences. Finally, while our model is tailored to PD gait patterns, its applicability to other abnormalities remains an area for future exploration.